Energy Conversion in High Enthalpy Flows and Non-equilibrium Plasmas

Kraig Frederickson[1], Sergey Leonov[2], Munetake Nishihara[3], Evgeny Ivanov[4], Igor V. Adamovich[5], Walter R. Lempert[6], and J. William Rich*[7]

Michael A. Chaszeyka Nonequilibrium Thermodynamics Laboratories,
Department of Mechanical and Aerospace Engineering
The Ohio State University, 201 W. 19th Ave., Columbus, OH 43210

Abstract

Recent developments in the study of very high energy non-equilibrium fluid flows are reviewed. These are flows of molecular gases which exhibit substantial degrees of mode disequilibrium, specifically high energy in molecular vibrational and electronic modes, and high electron energies when the gases are weakly ionized. In contrast, the modes of molecular translation and rotation remain at lower energies. Attention is focused on high density, collision-dominated gases. Studies in two systems are presented: A small wind tunnel where an M = 5 steady air flow over small models is produced, and a flowing carbon monoxide gas laser, exhibiting very high energy loading of the vibrational quantum states. The development of non-intrusive optical diagnostics to measure vibrational and electronic state populations and rotational/translational mode temperatures in the flows, with high spatial and temporal resolution, is presented. Kinetic modeling and experimental validation studies in these environments are also discussed.

[1] Research Scientist
[2] Visiting Professor
[3] Research Scientist
[4] Research Scientist, Chaszeyka Fellow
[5] Professor
[6] Professor
[7] Professor Emeritus, corresponding author, rich.2@osu.edu, +1 (614) 292-6309

Report Documentation Page

Form Approved
OMB No. 0704-0188

1. REPORT DATE	2. REPORT TYPE	3. DATES COVERED
2014		**00-00-2014 to 00-00-2014**

4. TITLE AND SUBTITLE	5a. CONTRACT NUMBER
Energy Conversion in High Enthalpy Flows and Non-equilibrium Plasmas	5b. GRANT NUMBER
	5c. PROGRAM ELEMENT NUMBER
6. AUTHOR(S)	5d. PROJECT NUMBER
	5e. TASK NUMBER
	5f. WORK UNIT NUMBER
7. PERFORMING ORGANIZATION NAME(S) AND ADDRESS(ES) **Ohio State University,Department of Mechanical and Aerospace Engineering,201 W. 19th Ave,Columbus,OH,43210**	8. PERFORMING ORGANIZATION REPORT NUMBER
9. SPONSORING/MONITORING AGENCY NAME(S) AND ADDRESS(ES)	10. SPONSOR/MONITOR'S ACRONYM(S)
	11. SPONSOR/MONITOR'S REPORT NUMBER(S)

12. DISTRIBUTION/AVAILABILITY STATEMENT
Approved for public release; distribution unlimited

13. SUPPLEMENTARY NOTES
accepted for publication in Progress in Aerospace Sciences, 2014.

14. ABSTRACT
Recent developments in the study of very high energy non-equilibrium fluid flows are reviewed. These are flows of molecular gases which exhibit substantial degrees of mode disequilibrium, specifically high energy in molecular vibrational and electronic modes, and high electron energies when the gases are weakly ionized. In contrast, the modes of molecular translation and rotation remain at lower energies. Attention is focused on high density, collision-dominated gases. Studies in two systems are presented: A small wind tunnel where an M = 5 steady air flow over small models is produced, and a flowing carbon monoxide gas laser, exhibiting very high energy loading of the vibrational quantum states. The development of non-intrusive optical diagnostics to measure vibrational and electronic state populations and rotational/translational mode temperatures in the flows, with high spatial and temporal resolution, is presented. Kinetic modeling and experimental validation studies in these environments are also discussed.

15. SUBJECT TERMS

16. SECURITY CLASSIFICATION OF:			17. LIMITATION OF ABSTRACT	18. NUMBER OF PAGES	19a. NAME OF RESPONSIBLE PERSON
a. REPORT **unclassified**	b. ABSTRACT **unclassified**	c. THIS PAGE **unclassified**	**Same as Report (SAR)**	**46**	

Contents

1. Introduction

2. Nonequilibrium Flow Wind Tunnel Experiments

2.1. *Wind Tunnel Configuration*

2.2. *Flow and Discharge Characterization*

2.3. *Diagnostics*

2.3.1. *Schlieren System*

2.3.2. *PLIF System*

2.3.3. *Picosecond CARS Diagnostic System*

2.4. *Measurements*

2.4.1. *NO PLIF Measurements*

2.4.2. *CARS Measurements*

3. Laser Power Extraction from Hypersonic Flow

3.1. *Creating Total Population Inversions in CO by Chemical Reaction*

3.2. *Kinetic Modeling*

3.3. *Optically Pumped CO Laser Experiments and Kinetic Model Validation*

4. Conclusions

Acknowledgments

References

1. Introduction

The nonequilibrium of molecular modes of motion can play a major role in high speed flow fields, influencing dynamic forces, heat transfer, and radiative signatures in aerospace vehicles. In addition, such flows often are weakly ionized plasmas, with attendant electron-molecule energy transfer processes that figure in the study and development of high power gas lasers. Non-equilibrium is defined here as occurring in a fluid when one or more molecular or electron components have differing mean energies. Usual thermodynamic equilibrium does not pertain; the fluid energy content cannot be characterized by a single temperature. Such non-equilibrium can be created by a variety of processes, including shock heating, rapid supersonic expansion, radiative energy absorption, or the passage of an ionizing voltage pulse. If the fluid is isolated from further work interactions, the system will of course decay ("relax") to thermal equilibrium, but with continuing rapid energy input, quasi-steady state non-equilibrium can be maintained.

The Non-equilibrium Thermodynamics Laboratories (NETL) at Ohio State conduct studies of a variety of non-equilibrium flows of particular aerospace interest. Of special interest are weakly-ionized environments where the slow-relaxing vibrational energy modes and the free electrons have much higher energies than the translational and rotational modes of flowing gases. We review here two on-going projects involving such environments. The first is basic study in a small scale Mach 5 non-equilibrium flow wind tunnel. In the tunnel, the vibrational energy of air species is loaded by an electric discharge in the plenum, and the energy content is controlled by adding relaxer species downstream. The second project is an application of non-equilibrium flow studies. This project is to extract power from a hypersonic air flow reacting with carbon at high altitude. This involves the development of a high power laser using carbon monoxide produced by reacting entrained air with carbon. The laser is to develop a total population inversion among its vibrational quantum states.

2. Nonequilibrium Flow Wind Tunnel Experiments

The wind tunnel is a small scale supersonic flow system, which can develop steady Mach 5 flows that can be sustained for several seconds. Turn-around times are short, enabling many test runs to be made each hour. With the non-equilibrium loading of the molecular vibrational modes, these are actually very high enthalpy flows, an environment which is usually achieved only in short duration hypersonic test facilities, such as shock tunnels. The long test times and short turn-around times here are important, enabling relatively rapid development of non-intrusive optical diagnostics which would be difficult to achieve in larger, short-pulse facilities. A detailed description of the system is given in Ref. [1].

The goals of this program are multi-fold. We wish to:

1. Obtain experimental data on molecular energy transfer mechanisms and rates to enable predictive modeling of high-speed non-equilibrium flow fields.
2. Develop instrumentation to measure temperature, vibrational populations, and species concentrations in air flows. The instrumentation includes high frame rate nitric oxide planar laser induced fluorescence (NO PLIF), high frame rate nitric dioxide molecular tagging velocimetry (NO_2 MTV), picosecond coherent anti-Stokes Raman spectroscopy

(psec CARS), two-photon absorption laser induced fluorescence spectroscopy (TALIF), and Thomson scattering.

3. Demonstrate use of such instrumentation to obtain data in short duration hypersonic flow facilities, i.e., in large scale shock tunnels and blow-down wind tunnels.
4. Develop methods of actively influencing flow field energy storage, energy transfer, and aerodynamic control.

Considerable progress towards achieving these goals has been made. We review some of the more significant developments here.

2.1. Wind Tunnel Configuration

Fig. 1 shows schematic layouts of this wind tunnel. The top drawing is the side view of the system; the bottom drawing is an enlarged top view of the tunnel plenum only. The tunnel walls are made of heavy acrylic plastic. The low gas kinetic temperatures in the flow permit this, despite the very high energy loading of some of the internal molecular modes. Gas flow is from left to right in the figure. Upstream, dry air or nitrogen gas is injected into a flowing plenum section. Gases are supplied at plenum pressures of P_0 = 0.5-1.0 atm. Steady-state non-equilibrium supersonic flow in the wind tunnel is produced by sustaining a high-pressure electric discharge in the plenum. Here, two pairs of electrodes are arranged to provide orthogonal current flow paths. These electrodes create two fully overlapping discharges in a rectangular cross section channel 1 cm in height and 4 cm wide (see Fig. 1). The first is a transverse, nanosecond pulse discharge sustained between two plane dielectric barrier electrodes flush mounted in the top and bottom walls of the discharge section, and operated at a high pulse repetition rate of ν = 100 Hz. The second is a transverse dc discharge sustained between two copper plate electrodes 4 cm long with a height of 1 cm, mounted in the side walls of the discharge section.

The main purpose of the two overlapping discharges is to generate stable non-equilibrium plasmas at high plenum pressures and discharge energy loadings. The repetitive nanosecond pulse discharge is operated using a high peak voltage (up to 30 kV), short pulse duration (5 nsec) pulse generator. Volume ionization in the discharge section is generated during each high-voltage pulse, after which the voltage is turned off before ionization/heating instability has time to develop. Between the ionizing pulses, energy is coupled to the flow by the dc discharge, sustained in the ionized flow created by the pulser. The dc voltage is deliberately kept low below breakdown threshold, typically below 4-5 kV, to preclude development of a self-sustained (i.e., independent of pulsed ionization) dc discharge in the high pressure flow, which would result in instability development and arcing. The bulk of the power loading into the flowing gas is provided by the dc discharge; the pulsed discharge provides the ionization. The dc voltage can be selected to input energy into the various internal energy modes; typically, it is set to maximize energy into the molecular vibrational modes.

Previously, this approach has been used in our work to sustain high- power discharges in a Mach 3-4 MHD wind tunnel [2, 3] and in an electrically excited gas dynamic oxygen-iodine laser [4]. In the present experiments, the repetitively pulsed discharge is operated for up to several seconds, and the dc discharge is operated for 0.5–1.0 s. The reduced electric fields in the two discharges are significantly different, $(E/N)_{peak}$ ~ 300 Td in the nanosecond pulsed discharge and

E/N ~ 10 Td in the dc discharge (1 Td = 10^{-17} V·cm^2). At these conditions, a significant fraction of input power in the pulsed discharge is spent on electronic excitation, dissociation, and ionization of the test gases, while nearly all input power in the dc discharge (up to ~ 80–90% [5]) is stored in the vibrational energy modes of nitrogen and oxygen, with fairly little power going to translational/rotational modes, i.e., to heat. Due to a very long N_2 vibrational relaxation time (~7 atm· s) at near-room temperature [6], this approach can create essentially vibrationally frozen nitrogen and air flows in the supersonic test section, with vibrational temperature considerably exceeding the translational/rotational mode temperature. The system is in no sense an "arc tunnel". Unlike an arc tunnel, the plenum excitation creates a glow-type electric discharge, highly non-equilibrium, with relatively low gas kinetic heating.

Optical access to the flow in the discharge section is provided through multiple optical windows, including two 1.5-inch diameter BK-7 glass windows in the side walls of a separate optical diagnostics section, which can be placed between the discharge section and the nozzle (see Fig. 1), and a 2-inch diameter UV-grade fused silica window, which can be installed in the back wall of the discharge section. Recently, the optical diagnostics section has been used to measure vibrational temperature of nitrogen downstream of the discharge section, using a picosecond CARS system [7]. The 2-inch optical access window has been used to take Intensified Charged-Coupled Device (ICCD) camera images and photographs of the discharge, as well as UV/visible emission spectra (nitrogen second positive bands) used for translational/rotational temperature inference in the discharge. The emission spectra have been taken using an optical multichannel analyzer (OMA) with a Spectra-Physics 0.25 m spectrometer. When the 2-inch window is used, the flow enters the discharge section at 90 degrees to the wind tunnel axis, which may adversely affect the flow quality in the plenum. Therefore, in the experiments when discharge images and emission spectra are not taken, the flow enters the plenum through the back wall of the discharge section.

Downstream of the discharge section, various gases can be injected into the main flow using a choked-flow injector with 20 injection ports in the top and bottom channel walls, 1 mm in diameter each, shown in Fig. 1. In the injector, the channel height is reduced to 5 mm to increase the flow Mach number and to improve mixing with the main flow. The flow Mach numbers in the discharge section and in the injector, estimated based on a quasi-one-dimensional isentropic flow theory, are M ~ 0.1-0.2 and M ~ 0.2, respectively. Gases injected into the main flow include oxygen, nitric oxide, hydrogen, and carbon dioxide, all diluted in nitrogen carrier. Oxygen can also be added to the main nitrogen flow excited in the discharge to create vibrationally excited synthetic airflow. Nitric oxide added to the main flow is used for NO PLIF measurements. Finally, NO, H_2, or CO_2 injection is used to accelerate the rate of vibration–translation (V–T) or vibration–vibration (V–V) relaxation in the flow vibrationally excited in the discharge, to control vibrational energy loading of the flow in the supersonic test section.

Downstream of the injector, the flow expands through an aerodynamically contoured two-dimensional Mach 5 nozzle, with a throat height of 1.6 mm. Top and bottom walls of the supersonic test section after the nozzle exit diverge at a 1.5 degree angle each to provide boundary-layer relief. The static pressure in the supersonic section is measured using a wall pressure tap in the side wall at the end of the nozzle. A 4 cm long, 5 mm diameter quartz cylinder model is mounted in the center of the 7 cm long supersonic test section, i.e., 3.5 cm downstream of the end of the nozzle. The model extends wall-to-wall and is held in place using extensions placed

inside circular recesses drilled in 2 x 2 in. UV-grade fused silica optical access windows flush mounted in the side walls of the test section. Two additional optical access windows, also 2 x 2 inches UV-grade fused silica, are flush mounted in the top and bottom test section walls, thus providing optical access to the supersonic test section from all four directions. The windows are used for NO PLIF measurements, schlieren visualization, and emission spectroscopy measurements.

Downstream of the test section, a supersonic diffuser with a 5 degree step angle is used to improve pressure recovery before the flow exits into an 8-in.-diam vacuum pipe, connected to a 110 ft^3 vacuum tank and a 200 cfm vacuum pump. At the baseline conditions, plenum pressure of $P_0 = 370 \pm 0.05$ torr, the test section static pressure is $P = 1.2 \pm 0.05$ torr, corresponding to a Mach number of $M = 4.55 \pm 0.03$. During the experiment, both the main flow through the discharge and the injection flows are controlled using solenoid valves. The main flow rate is calculated using a choked-flow equation, based on the plenum pressure and the nozzle throat area. Injection flow rates have been measured using a mass flow controller. At the baseline conditions, nitrogen at P_0= 0.5-1.0 atm, the mass flow rate through the tunnel is 7.5-15.0 g/s and the steady- state run time at the constant static pressure in the supersonic test section is 5-10 s. The runs can be repeated every few minutes.

2.2. Flow and Discharge Characterization

Fig. 2 plots the Mach number in the supersonic test section vs. the plenum pressure, inferred from wall static pressure measurements at the end of the Mach 5 nozzle. The static pressure was measured in the cold nitrogen flow (without the discharge in the plenum) for three different sets of conditions, (a) without a cylinder model in the test section, (b) with a 5 mm diameter cylinder model, and (c) with a 10 mm diameter model. It can be seen that, as the plenum pressure is increased, the Mach number measured without the model in the test section approaches the design Mach 5 value, M=4.5-5.0 at P_0=380-760 torr. One can also see that installing the 5 mm diameter model has a fairly minor effect on the static pressure and the Mach number, M=4.5-4.8 at P_0=380-760 torr. With the 10 mm diameter model in the test section, the Mach number decreases significantly, to M=4.0 at P_0=440-760 torr. As the cylinder model diameter is increased, the static pressure rise and the apparent Mach number reduction are most likely due to boundary layer buildup on the plane side walls of the tunnel, affected by the secondary cross flow [8], and its interaction with the model, which produces significant flow blockage.

These results are consistent with the predictions of CFD calculations using a hybrid, implicit unstructured fully coupled finite volume solver (US3D) [9,10] that solves the compressible, three-dimensional Navier-Stokes equations to compute the flow field. The code was developed and used to model the cold flow (with electric discharges off) in the tunnel [1, 9-10]. A subsonic inflow boundary condition is used for the nozzle [11]. Fig. 3 shows the code predictions for nitrogen flow at P_0=380 torr and T_0=300 K. The predicted side wall static pressure 4 cm upstream of the cylinder model is P=1.08 torr, which is close to the measured static pressure at this location, P=1.2 torr. It can be seen that the Mach number upstream of the 5 mm diameter cylinder model is about M=4.5, in good agreement with the Mach number inferred from the static pressure measurement. One can also see “bulges” developing in the side wall

boundary layers due to the secondary cross flow. However, approximately 50% of the test section width upstream of the cylinder is occupied with an "inviscid core" flow with M=4.5.

2.3. Diagnostics

We review here some of the principal diagnostics used to characterize the nonequilibrium flow features of this tunnel. Beyond the schlieren system, the laser diagnostic systems reviewed here were developed at NETL for this hypersonic nonequilibrium flowfield application; they have already been exported and used in larger test facilities in the United States.

2.3.1 Schlieren System

The shock wave standing in front of the cylinder model in the supersonic test section is visualized by schlieren diagnostics. The schlieren system uses a high-power green LED with a thermoelectric cooler as a continuous light source and a CMOS camera operated in video mode (exposure time 1.5 ms, frame rate 4 to 8 frames per second). Taking schlieren images is not synchronized with the discharge operation, but correct timing is controlled by partially overlapping the plasma image with the schlieren image on the camera. Optical access on all four sides of the test section enables taking schlieren images of the shock from two different directions, both parallel and perpendicular to the cylinder model axis (side view and top view).

2.3.2 PLIF System

The flow field in the supersonic test section is visualized by high frame rate NO PLIF, using a custom design, tunable burst-mode laser described in detail in Refs. [12,13]. The laser is capable of generating bursts of 10 to 20 pulses at the fundamental frequency of 1064 nm, at a high pulse-repetition rate, 10–500 kHz, burst repetition rate of 1 Hz, and pulse energy of up to 100 mJ/pulse. The laser is tunable over a wide range of wavelengths, using nonlinear wave mixing and a custom-design optical parametric oscillator. For high frame rate NO PLIF imaging, the laser-generated bursts of 10-20 pulses in the vicinity of 226 nm, at a pulse-repetition rate of 10-20 kHz (0.05 – 0.1 ms burst duration) and a pulse energy of ~ 0.3 mJ/pulse [14]. The laser is operated both in a broadband mode and in the injection-seeded mode, to produce narrow linewidth (~0.01 cm^{-1}) tunable output, providing access to NO ($X^2\Pi_{½},v' \rightarrow A^2\Sigma,v''$) absorption transitions. Nitric oxide is seeded into the flow through the injector in the subsonic part of the wind tunnel, as discussed previously, or through the short cylinder model in the supersonic test section, using a 20%NO–80%N_2 mixture. Baseline NO mole fraction in the main flow with subsonic injection was 0.3%. NO PLIF measurements have also been conducted in unseeded airflows using nitric oxide generated in the electric discharge in the plenum.

Injection-seeded (single-line) laser operation was used to pump NO on two different rotational lines of the $v' = 0 \rightarrow v'' = 0$ band, Q1 + P21 (J = 5.5) line at 226.17 nm and Q1 + P21 (J = 16.5) line at 225.88 nm, to measure the rotational temperature in the supersonic test section, as well as on a single rotational line of the $v' = 1 \rightarrow v'' = 1$ band, Q1 + P21 (J = 3.5) at 223.83 nm, to measure NO vibrational temperature. The laser sheet, approximately

2.5 cm wide, is directed through the supersonic test section vertically, using optical access windows in the top and bottom walls. NO fluorescence was collected at 90 degrees through the side window and detected by a PI-MAX UV-I CCD camera (Princeton Instruments) with a UV lens (f = 100 mm, Thorlabs). The camera gate was set at 1 ms to accumulate fluorescence signal after excitation by 10 pump laser pulses, with the laser operating at a 10 kHz pulse-repetition rate. To monitor the intensity distribution across the laser sheet, approximately 5% of the incident sheet was reflected off a glass plate placed 2 cm above the wind tunnel and directed into a cell filled with a Rhodamine 640 dye diluted in methanol. The fluorescence from the dye in the cell, between 570 to 600 nm, was recorded using a PIXIS 256E 1024 x 256 pixel CCD array camera (Princeton Instruments), thus yielding the laser sheet intensity distribution. The NO PLIF signal distribution was normalized on the laser sheet intensity distribution during post-processing of the experimental data. Emission spectra from the flowing afterglow in the supersonic test section have been taken using the same OMA system as discussed previously. Afterglow images were taken using either the PI-MAX ICCD camera or the Andor iStar ICCD camera.

2.3.3 Picosecond CARS Diagnostic System

Picosecond Coherent Anti-Stokes Raman Scattering (CARS) spectroscopy has been used for the direct measurement of the ro-vibrational distribution functions of nitrogen. CARS is a four wave mixing spectroscopic technique which has been used extensively for thermometry and species concentration measurements of combustion and other gas phase reacting and non-reacting flows [15,16]. CARS involves the interaction of three input photons, termed pump, Stokes, and probe, with a molecule, resulting in the generation of a signal photon. If the pump/Stokes photons have a frequency difference corresponding to an internal degree of freedom (generally rotational or vibrational), a strong coherent (laser-like), "resonant" signal is produced in a direction determined by what is known as the "phase-matching" criteria. All data presented in this work used vibrational Q-branch ($\Delta J = 0$) transitions.

The CARS signal intensity, I_{CARS}, has a linear dependence on the Stokes laser intensity, I_{Stokes}, while scaling quadratically with the magnitude of the CARS susceptibility (proportional to number density, $|\chi_{CARS}| \propto N$), i.e. $I_{CARS} \propto I_{Stokes} \cdot N^2$. These effects are accounted for in the data processing. Normalizing the CARS intensity by a non-resonant background (NRB) spectrum captured in argon accounts for the variation in the intensity profile of the Stokes laser. It was experimentally determined that the average NRB profile was very stable over the course of a day, so one 200-shot average NRB spectrum was used to normalize the data captured each day. After the data normalization, the square root of the intensity is taken to account for the quadratic dependence on number density; all spectral data plotted below is this square root of normalized intensity. For measurement of an effective vibrational "temperature", T_v, the CARS cross section must also be accounted for, which for low vibrational levels of nitrogen scales approximately as $(v''+1)^2$ [7]. Since the square root of the data has already been taken, dividing the integral of each peak by (v"+1) yields the relative vibrational population in each level.

For the hypersonic nonequilibrium flow tunnel, the Unstable-resonator Spatially Enhanced Detection (USED) phase matching geometry [17,18] has been employed. For this geometry the single 532 nm pump/probe beam is enlarged with a telescope and the center portion of the beam is removed, creating an annulus. This beam is then combined coaxially with the

Stokes beam by a dichroic mirror, similar to a collinear alignment except that there is no spatial overlap because the Stokes beam occupies the void created within the pump/probe beam. After the beams pass the focusing lens, the two regions of the annular pattern remain spatially separated until they arrive very near to the focal region; it is within this small overlap volume that CARS signal generation occurs. According to the phase matching criteria, the generated CARS signal appears as a ring outside of the pump/probe beam. This phase matching scheme is primarily chosen due to concerns about potential beam steering that would occur for measurements performed in the vicinity of the characteristic bow shock produced by test objects in the Mach 5 section of the flow, as well as a desire to perform measurements as close as possible to the test object surface. There is a small sacrifice in spatial resolution, relative to the more common folded BoxCARS geometry, but this is not significant for the measurements reported here. The transverse spatial resolution for our system is on the order of 50 μm; a measurement of the longitudinal resolution, performed by scanning a glass flat in the vicinity of the CARS measurement volume and observing the non-resonant background signal, indicates that >95% of the signal generated comes within a 3 mm length at the beam focus, as compared to ~1 mm or less for BoxCARS, and 1-2 cm for collinear CARS (determined in the same manner).

The broadband Stokes beam is generated with a NETL-developed dye laser, patterned after Ref. [19], which employs side-pumped oscillator and pre-amplifier cells, followed by an end-pumped final amplifier cell (note there is no output coupler). The combination of a half-wave plate and thin film polarizer allows for adjustment of the ratio between energy pumping the dye versus the energy in the CARS pump / probe beam. Dye laser energy efficiency is as high as 10%. For this work, mixtures of Rhodamine 640 (R640) and Kiton Red 620 (KR620) were used. The dye laser output is centered near 604 nm, with a full width at half maximum (FWHM) of approximately 5-6 nm [20].

The dye laser is pumped by an Ekspla SL-333 Nd:YAG laser, as can be seen in Fig. 4, which shows a schematic of the CARS experimental arrangement. The nearly transform limited YAG outputs pulses of approximately 150 picoseconds in duration, with variable energy output of up to 120 mJ/pulse at 532 nm. The choice to use a picosecond (psec) system is motivated by several reasons, including enabling time-resolved measurements at nsec and sub-nsec time scales, as well as lowering necessary pulse energies, reducing the risk of window damage. After the dichroic mirror, which creates the 532 nm / 607 nm annulus, the beams are focused into the test section with a 250 mm focal length lens. After the focal point, located in the center of the wind tunnel, the beams are re-collimated using a 100 mm focal length lens.

After the collimating lens, a series of long-wavelength-passing dichroic mirrors reflect the ~473 nm CARS beam while dumping the pump / probe and Stokes beams. Finally, the CARS signal passes through a short-pass filter, with a cutoff wavelength of 503 nm, and is focused by a 100 mm lens onto the slit of a 0.75 m Andor Shamrock 750 spectrometer. At the exit plane of the spectrometer, a relay lens magnification system, comprised of two Nikon F-mount lenses, a 35 mm lens attached to the spectrometer and an 80-200 mm telephoto lens attached to the camera, provides variable spectral resolution magnification. For the work presented, the lens was set to give a ~2.3x magnification, which resulted in a spectral resolution of ~0.4 cm^{-1} when used with a 3600 lpmm grating. This is sufficient to partially resolve the rotational structure in room temperature Q-branch spectra of nitrogen, as will be demonstrated in the next section. The camera used is an Andor Newton EM-CCD; the 1600 by 400 pixel sensor array is cooled to -90^0 C, with the EM gain set to 150. The camera and spectrometer are

interfaced to a lab computer for data recording. The entire picosecond CARS system is placed on a custom built cart, allowing the entire setup to be easily transported between experimental facilities.

2.4. Measurements

We show in this section some typical nonintrusive measurements in the tunnel and model flow fields, using the diagnostics reviewed above.

2.4.1 NO PLIF Measurements

Fig. 5 shows schlieren images of a bow shock in front of a 5 mm diameter cylinder model in the supersonic test section (top view and side view). These images were taken in cold nitrogen flow at P_0=350 torr, without the discharge in the plenum. At these conditions, the shock stand-off distance is 1.2 ± 0.05 mm, with the shock extending across the flow over approximately 20 mm, i.e. over about half of the test section width. Figure 5 also shows synthetic schlieren bow shock images (contour plots of density gradient) predicted by the 3-D compressible Navier-Stokes code. It can be seen that the shock stand-off distance and the spanwise extent predicted by the code are in good agreement with the experiment.

Fig. 6 compares NO PLIF images of the bow shock flow of Fig. 5 with Mach number distribution (left) and the temperature distribution (right) predicted by the 3-D compressible Navier-Stokes flow code for nitrogen at P_0=350 torr (without the discharge in plenum). It can be seen that the code predictions are in good qualitative agreement with the flow visualization images. In particular, bow shock shape and stand-off distance, as well as the size of the wake behind the model are reproduced well by the flow code.

Fig. 7 shows two-dimensional rotational temperature distributions in a nitrogen flow behind the bow shock at P_0=370 torr, inferred from the intensity ratio of two single-line PLIF images, J=5.5 and J=16.5. The temperature distributions are shown for two cases, cold flow (no discharge in the plenum), and pulsed / DC discharge excited flow (ν=100 kHz, U_{PS}=4.5 kV). To calculate the temperature distributions, intensity ratios were calculated and rotational temperature was inferred for five pairs of NO PLIF images, averaged over 10 laser pulses each (both for J=5.5 and for J=16.5). From Figure 7, it can be seen that temperatures inferred at the stagnation point are T=300±30 K in the cold flow and T=500±190 K in the flow excited by the discharge in plenum. Although Joule heating of the flow in the discharge contributes to higher stagnation point temperature with the discharge on, this result also suggests significant vibrational relaxation of nonequilibrium nitrogen flow, excited by the discharge in the nozzle plenum, behind the shock. Vibrational relaxation of the flow in the shock layer can be quantified by further measurements of nitrogen vibrational temperature behind the shock, using psec CARS diagnostics, which are discussed in the following subsection. Temperature inferred in the free stream is subject to significant uncertainty due to very low fluorescence signal in this region. In the present work, the two rotational transitions were chosen for best temperature measurements sensitivity behind the bow shock. Note that temperature inferred in the “shadow” region below the cylinder model cannot be considered accurate, since laser beam lensing by the model may well cause saturation of the absorption transitions and result in a significant error in the

temperature. Finally, temperature inferred in the wake behind the model cannot be inferred with any certainty due to a very low fluorescence signal in this region, both in J=5.5 and J=16.5 images.

Fig. 8(a) shows an NO PLIF image obtained when the pump laser was tuned to the NO absorption transition NO(X,v′=1 → A,v″=1), $Q_{11}+P_{21}$ (J=3.5) at 223.83 nm. The laser pulse repetition rate was 10 kHz, and the image was accumulated over 10 laser pulses. The nitrogen flow at P_0=370 torr was excited by a pulser / sustainer discharge (ν=100 kHz, U_{PS}=4.5 kV) and seeded with 0.3% of NO. In Figure 8(a), the v′=1 fluorescence signal intensity near stagnation point is approximately 30 times lower compared to the fluorescence intensity of v′=0 in the same region. In nitrogen flows excited by the electric discharge in the nozzle plenum and seeded with small amounts of NO, bright spontaneous emission on NO($A^2\Sigma \rightarrow X^2\Pi$) transitions (γ bands) was found to overlap with the NO PLIF signal due to rapid collisional energy transfer from the $N_2(A^3\Sigma)$ state generated in the discharge to the NO($A^2\Sigma$) state, $N_2(A^3\Sigma) + NO(X^2\Pi) \rightarrow N_2(X^1\Sigma) + NO(A^2\Sigma)$, with a room temperature rate coefficient of $k=6.9\cdot10^{-11}$ cm^3/s [21]. However, the NO mole fraction of 0.3%, used to obtain the NO(v=1) PLIF image of Fig. 8(a), appears sufficient to quench the $N_2(A^3\Sigma)$ state in the subsonic section completely, and no spontaneous emission of NO was detected at these conditions. Note that the intensity distribution in the NO(v=1) PLIF image is nearly uniform, indicating that NO vibrational temperatures in the free stream and behind the bow shock are fairly close.

Fig. 8(b) shows a two-dimensional NO vibrational temperature distribution inferred from the intensity ratio of the NO PLIF images from (v´=0, J=5.5) and (v´=1, J=3.5), taking into account the difference in the laser pulse energies, Frank-Condon factors, rotational level populations, and Einstein coefficients for spontaneous emission. The average NO vibrational temperature inferred along the flow centerline in the free stream is T_v(NO)=1000 K±170 K. Note that the apparent NO vibrational temperature exceeding 2000 K, inferred below the cylinder model (see Fig. 8(b)), are affected by low signal-to-noise ratio in this region (in the "shadow" of the model).

Figs. 9 and 10 show split comparison of the temperature fields inferred from NO PLIF measurements with the CFD model predictions, with and without the pulser / DC discharge operating in plenum. For the conditions with the discharge on, comparison with CFD calculations was done for T_0=500 K and T_{v0}=1700 K, close to the temperatures measured in plenum by psec CARS (see following subsection). As can be seen from Figs. 9 and 10, the results of NO PLIF thermometry measurements and CFD modeling calculations predictions show good agreement. The results of the calculations also demonstrated that energy loaded by the discharge into the vibrational mode of nitrogen remains "frozen" throughout the entire flow, including flow behind the bow shock, consistent with the CARS measurements, which we review below.

2.4.2 CARS Measurements

Pure Nitrogen Flow, No Discharge

These measurements focus on both translational / rotational temperature, T_{rot}, as well as the "first-level" vibrational temperature, T_{vib}, defined as

$$T_{vib} = \frac{\theta_{vib}}{\ln[n_0/n_1]}\ , \tag{1}$$

where for nitrogen, θ_{vib} = 3353 K is the energy difference between vibrational levels v = 0 and v = 1 in temperature units. While under low resolution the spectral output of the Stokes beam from the modeless dye laser appears very similar from one shot to the next, higher resolution reveals significant shot-to-shot spectral profile variation. To partially mitigate this, 20 single-shot spectra are averaged together. An example of this can be seen in Fig. 11, taken at P_0 = 370 torr and nominal room temperature, T ~ 300 K. For rotational temperature inference, after the averaging is performed, the spectrum is fitted with the Sandia CARSFT least-squares fitting code [22]. The resulting nitrogen best fit rotational temperature for the spectrum shown in Fig. 11 (b) is $T_{rot}(N_2)$ = 322 K, with precision equal to +/- 20 K. For vibrational temperature inference the v = 0 and v=1 bands, which are well isolated spectrally, are numerically integrated, which upon division by v″+1 to correct for the cross section (for assumed harmonic potential), yield the v = 0 and v=1 level populations

Pulser-Sustainer Discharge, with Relaxer Injection

Fig. 12 shows a pair of N_2 CARS spectra obtained from operation of the pulser-sustainer discharge, with a DC power supply voltage (V_{PS}) of 4.5 kV. The dash-dotted black curve corresponds to a baseline case of pure nitrogen flow at 300 torr and the solid blue curve shows the spectrum when 1 torr partial pressure of CO_2 is injected downstream of the discharge, approximately 9 cm (~2 msec) upstream of the CARS measurement location. It is clear that there is a significant difference between the two conditions. For no relaxer injection, the flow is extremely non-equilibrium, with a vibrational temperature of nearly 2000 K, while the inferred gas rotational/translation temperature is T_{rot} ~ 450 K. With only 1 torr partial pressure of carbon dioxide injected, nearly all the vibrational energy has been removed from the nitrogen, evidenced by the nearly equilibrated T_{vib} = 815 K and T_{rot} = 630 K.

Five different species (carbon dioxide, nitric oxide, hydrogen, oxygen and nitrogen) were injected over a range of partial pressures. These gases were chosen because their rates for nitrogen vibrational relaxation vary by several orders of magnitude. Fig. 13 plots both the nitrogen vibrational and rotational / translational temperatures measured in these mixtures versus the partial pressure of the injected species. It can be seen that the addition of oxygen to the discharge-excited nitrogen (solid red curve), up to 20% mole fraction (nearly "synthetic air"), does not cause a significant change in either the vibrational or rotational gas temperature, due to the low vibration-vibration (V-V) energy transfer rate coefficient, $N_2(v=1) + O_2(v=0) \rightarrow N_2(v=0) + O_2(v=1)$, $k_{VV} = 3\cdot10^{-17}$ cm^3/sec at T_{rot} = 450 K [23]. For injection of 60 torr oxygen, the characteristic time for nitrogen V-V relaxation, $\tau_{VV} \sim 1/k_{VV}n_{O2}$ ~ 17 msec, is significantly longer than the ~2 msec flow residence time between the injection location and the CARS measurement region. The characteristic time for V-T relaxation for N_2-O_2 is even longer.

As can also be seen in Fig. 13, carbon dioxide (magenta dash-dot curve), which is known to be an extremely rapid relaxer of nitrogen vibrations, exhibits the most rapid rate of relaxation. Even at the lowest injection partial pressure, P_{CO2} = 0.25 torr, a substantial reduction of nitrogen vibrational temperature, by more than 450 K, is observed, as well as a corresponding increase in nitrogen rotational temperature by 50 K. The rate coefficient for V-V energy transfer, $N_2(v=1) + CO_2(000) \rightarrow N_2(v=0) + CO_2(001)$, at T_{rot} = 450 K, is very high, $k_{VV} = 4.5\cdot10^{-13}$ cm^3/sec [23]

($\tau_{VV} \sim 1/k_{VV}n_{CO2} \sim 70$ μsec for CO_2 partial pressure of only 1 torr). CO_2 vibrationally excited in collisions with nitrogen relaxes via rapid intramolecular V-V energy transfer to ν_2 (010) and ν_1 (100) modes, with subsequent rapid V-T relaxation.

Injection of nitric oxide and hydrogen exhibit similar behavior to carbon dioxide, although on a slower time scale. The rate coefficient of V-V energy transfer from nitrogen to nitric oxide, $N_2(v=1) + NO(v=0) \rightarrow N_2(v=0) + NO(v=1)$, is $k_{VV} = 3.4 \cdot 10^{-15}$ cm^3/sec at 450 K [24] ($\tau_{VV} \sim 1/k_{VV}n_{NO} \sim 2$ msec for NO partial pressure of 5 torr, comparable to the flow residence time). The V-T relaxation rate coefficient for N_2-H_2, $N_2(v=1) + H_2 \rightarrow N_2(v=0) + H_2$, is $k_{VT} = 6.1 \cdot 10^{-16}$ cm^3/sec at 450 K [25] ($\tau_{VT} \sim 1/k_{VT}n_{H2} \sim 6$ msec for H_2 partial pressure of 10 torr). Using the temperature dependence suggested in [26], this rate increases to $k_{VT} = 1.3 \cdot 10^{-15}$ cm^3/sec at $T = 550$ K ($\tau_{VT} \sim 3$ msec). Similarly to N_2-O_2, the V-V energy transfer for N_2-H_2 is extremely slow, due to a significant difference in vibrational quanta [27].

Injection of non-excited nitrogen was also performed; although the V-V energy transfer rate coefficient for nitrogen, $N_2(v=1) + N_2(v=0) \rightarrow N_2(v=0) + N_2(v=1)$, is relatively high, $k_{VV} = 1.5 \cdot 10^{-14}$ cm^3/sec at room temperature [28] ($\tau_{VV} \sim 1/k_{VV}n_{N2} \sim 0.5$ msec for injection N_2 partial pressure of 5 torr), the resonant energy transfer process simply results in the redistribution of N_2 vibrational energy amongst the "discharge loaded" and "cold injected" molecules, but the energy remains "locked" in the nitrogen vibrational mode.

As the results of Fig. 13 indicate, energy extraction from the nitrogen vibrational mode results in an increase of the gas temperature, i.e. thermalization of the vibrational energy as the discharge-loaded flow is equilibrated. Fig. 14 plots the average total nitrogen translational/rotational + vibrational energy per molecule as a function of partial pressure of the injected species for all of the conditions shown previously in Fig. 13. As the figure demonstrates, within the experimental uncertainty, the total nitrogen rotational, translational, and vibrational energy is conserved. This indicates that any inter-species V-V transfer is followed by rapid V-T relaxation, with a result that there is negligible energy storage in the vibrational modes of injected species.

Measurements in a supersonic flow

Finally, measurements of vibrational temperature in the supersonic section have also been performed [7]. These measurements are especially challenging due to very low free-stream static pressure, $P_0 = 1.2$ torr, measured using a wall pressure tap at the end of the nozzle. As mentioned, a 5 mm diameter quartz cylinder is positioned in the supersonic flow, which creates a bow shock as shown previously in Figs. 5-10. The CARS spectra in Fig. 15 (a) are eight-shot averages, collected both in the supersonic free-stream and behind the bow shock for 300 torr pure N_2 in the plenum with no discharge. The difference in signal level results from the different number densities present in the two measurement locations; the spectra also demonstrate typical signal-to-noise levels for this arrangement. The plots in Fig. 15 (b) and (c) show ten-shot average spectra, collected in the supersonic free-stream and behind the bow shock, respectively, for 300 torr N_2 in the plenum, with the pulser-sustainer discharge in operation (sustainer $V_{PS} = 4.5$ kV). Electromagnetic interference (EMI) caused by the nsec pulser can be clearly seen in both spectra, and becomes increasingly problematic as signal levels decrease. The significant reduction in the ground vibrational level signal strengths for both of these spectra (compared to the "no-discharge" data acquired at each location) can be attributed to both a reduction in total

number density, due to gas heating from the discharge, as well as significant population loss to excited vibrational states. The ratio of the integrated square-root of peak intensities is used to determine the first-level nitrogen vibrational temperatures, as previously described.

Due to the quadratic scaling of CARS signal intensity to the density, as previously mentioned, the integrated square-root of the CARS signal gives an estimate of local number density. This can be used to determine if the measurement volume is upstream or downstream of the shock location, due to the significant rise in density as the flow traverses the shock. Spectra captured without the discharge in operation, such as those seen in Fig. 15 (a), are collected at various locations upstream of the cylinder, and the square-root of the spectral peaks are integrated to give an estimate of local number density. The results are shown in Fig. 16 (a), where the black "x" symbols are for pulser-sustainer discharge operating in 300 torr pure N_2 flow, and the red crosses are recorded with 0.25 torr CO_2 injection, as previously described. As the plot indicates, a sharp rise in density occurs 1.0 mm upstream of the cylinder surface. The cluster of data points captured at x = -1.00 mm (number density ~10 in arbitrary units), represent the free-stream position directly adjacent to the shock front. Moving downstream, measurements captured at x = -0.99 mm, -0.98 mm, and -0.95 mm, shown as the next three black "x" symbols on the plot, demonstrate much higher densities, indicating the measurement region has moved beyond the shock location.

As mentioned above, shock stand-off distance detected, 1.0 mm, is somewhat smaller than measured in our previous experiments using a 4 cm long, 5 mm diameter cylinder, supported at the tunnel sidewalls, 1.2 mm [1]. This may be explained by the effect of finite cylinder length, which has been studied in a Mach 4 flow in a shock tube experiment [29]. In [29], it was shown that the ratio of stand-off distance to the cylinder diameter, *d/D*, tends to decrease as the cylinder length-to-diameter ratio, *l/D*, is reduced below *l/D* = 4. This effect is primarily due to flow three-dimensionality, i.e. spanwise flow behind the bow shock. At the present conditions, *l/D* = 7.5 mm / 5 mm = 1.25. The number densities measured behind the shock are nominally 3-4 times higher than those measured in the free-stream, somewhat less than the bow shock density jump of 5.1, predicted by a 3-D compressible Navier-Stokes flow code for a cylinder model extending wall-to-wall [1]. The density ratio across the shock may be also affected by the three-dimensionality of the flow over the short cylinder model used in the present work.

The plot in Fig. 16 (b) shows the inferred $T_v(N_2)$ for several locations both in the free-stream and behind the shock. These data are taken with the pulser-sustainer discharge operating in 300 torr N_2 in plenum, with and without 0.25 torr CO_2 injection. Both with CO_2 injection and without injection, vibrational temperatures inferred behind the shock are very similar to those observed in the free-stream. As the recovery pressure behind the shock is significantly lower than the plenum pressure, vibrational relaxation beyond that present in the relatively high density subsonic flow does not occur. The vibrational temperature inferred for the case of 0.25 torr CO_2 injection is close to the value inferred in plenum at the same conditions, $T_v \sim 1450$ K. The vibrational temperature for pure N_2 without injection is ~150 K less than the value measured in plenum at the same conditions, $T_v = 1900$ K, a difference of less than 10%. Significant spread in the data is observed, primarily due to the rather low signal-to-noise levels present due to the EMI effects from the nsec pulser previously mentioned, as well as the general difficulty of very low CARS signal levels in these extremely low density flows.

In summary, these nonequilibrium flow studies demonstrate it is possible to make detailed measurements of vibrational energy content and translational and rotational mode temperatures in a hypersonic flow. The high spatial resolution along the small stagnation streamline behind the bow shock in the M ~ 5 flow of Fig. 16, for example, is noteworthy. In this environment, both vibrational "temperature" and translational/rotational mode temperature are measured with a spatial resolution > 0.1 mm. Also, these data can be acquired in short times. While the averages shown require times ~ 1 sec, useable single shot data can be acquired within a few nsec. Finally, we note that these methods can be extended to measurement of much higher quantum state populations in other nonequilibrium flows.

3. Laser Power Extraction from Hypersonic Flow

We discuss here an application of nonequilibrium flow research, which addresses the extraction of laser power from a hypersonic air flow reacting with carbon at high altitude. What is envisioned involves the following elements:

1. Entraining atmospheric air at high altitude in a hypersonic flow channel.
2. The entrained oxygen in the air reacts with carbon to produce carbon monoxide (CO) which is in high energy excited quantum states. These internal quantum states are in the CO vibrational mode, and, possibly, the CO electronic modes of molecular motion.
3. It is desired to produce the excited CO with a population inversion among some of the quantum states. Such a nonequilibrium environment is known to develop powerful laser gain. It would then be possible to extract infrared or ultraviolet laser power from the excited CO in the flow.

This is a major application of nonequilibrium flow research, and considerable progress has been made, which is reviewed here. We note that a long history of earlier development has shown that vibrational-mode-excited CO has produced the most powerful and efficient continuous wave (c.w.) lasers known that are scalable to very high steady infrared powers. Efficiencies as high as 50% were reported by Grigor'yan *et al* [30] and powers up to 200 kW have been obtained by Dymshits *et al* [31] in c.w. systems operating on the fundamental bands. Overtone c.w. lasing was also achieved in similar systems by Bergman and Rich [32], with efficiencies up to 5% reported by Utkin *et al* [33]. Many of these systems have recently been reviewed in detail by Ionin [34].

The mechanism creating the population inversion in these lasers was first described by Rich [35]. The lower quantum levels of the vibrational mode of CO are excited by inelastic collisions with the discharge electrons. Energy is then rapidly redistributed among the vibrational states by exchange of vibrational quanta in CO–CO inelastic collisions (so-called vibration-to-vibration, or "V–V" exchange collisions). When the mean energy in the vibrational mode exceeds the mean energy in the 'external' modes of molecular translation and rotation, an extremely non-Boltzmann distribution of population is maintained among the CO vibrational levels, in accordance with the basic theory of Treanor *et al* [36]. The distribution is characterized by significant overpopulation of the higher vibrational quantum levels; in most cases, there are not total population inversions between levels. Nevertheless, such "partial

population inversions" can lead to the powerful lasers noted above. These inversions are enhanced by either increasing the energy stored in vibration, or by decreasing the energy in the molecular translational and rotational modes, i.e. by decreasing the gas kinetic temperature. The most efficient lasers therefore cool the gases to cryogenic temperatures. They use a glow-type electric discharge to provide the vibrational excitation source, and rely on either wall-cooling or supersonic expansion to cool the discharge gases.

In the present program, CO is created by a chemical reaction, and the nascent CO reaction product is already in vibrationally excited quantum states. The study reviewed here is to address the following issues:

1. Can CO generated by reaction of oxygen with carbon produce a total population inversion in a fast flow, at the relatively high temperatures and gas densities typical of these flows?
2. Can the inversions be maintained in the presence of N_2, residual O_2, and other reaction products in the flow?
3. Can this kinetics be studied experimentally in a small scale laboratory environment?

3.1 Creating Total Population Inversions in CO by Chemical Reaction

There are two chemical reactions known to produce total population inversions among the vibrational quantum states of the CO molecule. The first is a reaction between oxygen atoms and carbon monosulfide,

$$O + CS \rightarrow CO\ (v > 0) + S \tag{2}$$

and the second is the reaction of carbon atoms and oxygen molecules,

$$O_2 + C \rightarrow CO\ (v > 0) + O\ . \tag{3}$$

Here, CO (v > 0) indicates CO in vibrationally-excited quantum states. The first reaction is the well-known "chemical CO laser" reaction, and has a long history and a demonstrated record of producing powerful laser action. In such CO lasers, mixtures of O_2 and CS_2 are typically processed by an electric discharge to produce the free radical O and CS reactants. The nascent CO (v > 0) product is in a total population inversion. Fig. 17, taken from the review by Djeu [37], shows these populations, wherein the ratio of the population of the v^{th} vibrational quantum state, N_v, to the first quantum state, N_1, is plotted against vibrational quantum number, v. The striking total inversion is evident, with the lowest states essentially unpopulated, and populations reaching a maximum at v ~ 12.

Interest for the present program centers about the second reaction, which can utilize atmospheric O_2. Very recent theoretical calculations [38] for this reaction predict that total inversions similar to those of Fig. 17 can be created with activation energies less than 0.5 eV. This prediction has been confirmed by recent crossed O_2 – C molecular beam experiments [39], which show a large reactive scattering cross section, with a total inversion extending up to at least v = 5. These results are extremely promising for creating a laser based on the C + O_2

reaction, but the task of the present nonequilibrium flow study is to see if these results can be developed into a working high speed flow laser, at hypersonic flow densities and temperatures.

3.2 Kinetic Modeling

An essential component of the project is the kinetic modeling of a potential large scale laser device. Supersonic flows with vibrational and electronic mode nonequilibrium, such as those presented in Section 2 above, are generally analyzed in the NETL group with kinetic modeling. Lasing action in CO – air mixtures lends itself to such modeling, inasmuch as a long history of development of high power CO lasers has led to a large data base of quantum-state-resolved vibrational energy transfer rates.

The kinetic model is based on the OSU CO optically pumped plasma model [40] and the CO laser field model of Rockwood and Brau [41]. The model also incorporates the quasi-one-dimensional equations of compressible flow, together with kinetic equations governing the population of each vibrational quantum level for each diatomic species in the laser gas mixture as a function of time ('master equation' modeling). It is assumed that at each point in the flow field, rotational-translational mode equilibrium pertains, so that a gas kinetic temperature can be defined at each point. Coupled with these equations is a set of laser field equations governing the stimulated emission intensity on each lasing vibrational transition as a function of time. The laser cavity model is a simple Fabry–Perot model, with the optical axis transverse to the flow direction. On each vibrational transition, lasing is assumed to occur on the vibrational–rotational transition with maximum gain. Input parameters to the calculation are initial gas species concentrations, the gas translational/rotational mode temperature, the flow channel geometry, cavity mirror reflectivities, cavity gain length, and cavity optical losses. The model predicts the laser output on each vibrational transition as a function of time.

We present one modeling case for the potential O_2 + C chemical laser. This case is to assess the possibility for the entrained air, reacting with carbon, to produce a powerful supersonic flow laser. In this case, the vibrationally excited CO is expanded into a supersonic nozzle. For this calculation, it is assumed that at an upstream point in the flow channel, sufficient carbon has been introduced into the flow to convert all available oxygen into vibrationally excited CO(v) by the O_2 + C reaction This forms a plenum at P = 200 Torr, T=500 K, 20% CO and 80% N_2. Downstream of the plenum, the gases are expanded through nozzle to an area ratio of $A/A^* = 4$, and a Mach number M = 3. The throat dimensions are 10 cm width x 0.5 cm height. The expanding portion of the supersonic section has a length of 10 cm. Assuming 50% of the reaction energy goes into CO(v), consistent with the predictions of theoretical calculations [38], the vibrational energy flux through the throat is 2.5 kW, with a mass flow rate of 20 g/sec. An idealized laser optical cavity is modeled, where mirrors are placed on the sidewalls of the nozzle, beginning at the nozzle throat, and extending downstream. This creates a transverse laser resonator cavity, 10 cm wide (across the throat), and 2 cm high. One mirror side is totally reflective, the other is 99% reflective, permitting 1% of the incident in-cavity laser radiation to be coupled out of the flow. We assume a single-pass cavity loss of 0.1% (0.01%/cm). The vibrationally excited CO entering the nozzle throat is assumed to be in a nascent reaction product population distribution similar to that shown in Fig. 17 above. This is modeled as a Gaussian distribution around v = 12, $\sim \exp[-(v-12)^2/10]$.

Figs. 18-20 show some results of this model calculation. In Fig.18, the relative

populations of each vibrational state, normalized by the ground state population, N_v/N_0, is plotted against vibrational quantum number, for several downstream positions in the nozzle, and with laser mirrors are not present in the cavity. At the throat, x=0, the strong total inversion centered at v=0 is seen. At the several further downstream shown positions, evolution of the vibrational distribution is displayed, with both levels both lower and higher than v=12 having increasing population. The process redistributing the vibrational state populations is almost entirely V-V inelastic collisional energy transfer which occurs with very large, near gas kinetic, collision rates. Despite this redistribution, however, some total inversions among the states persist down the flow channel, even to x=30 cm.

Figs. 19 and 20 plot several of the flow parameters down the nozzle, specifically Mach number, temperature, pressure, and velocity in Fig. 19 (without laser mirrors in the cavity); vibrational energy flux, laser gain, and output laser power in Fig. 20 (without and with laser mirrors in the cavity). It is seen that gain in the Mach 3 cavity, without the laser mirrors present, is ~ 1 %/cm at T=220 K (see Fig. 19). At these conditions, flow vibrational mode energy flux remains very nearly constant, ~ 2.5 kW (see Fig. 19), since vibrational relaxation time is much longer compared to the flow residence time. We note that the vibrational energy is retained in the CO vibrational mode even in the presence of the expected amount of molecular nitrogen; energy losses in collisions with the N_2 are included in the calculations. As shown in Fig. 20, adding the laser mirrors to the cavity results in laser action and rapid gain reduction to near transparency, caused by high peak radiation field buildup in the cavity. Predicted peak laser power flux is very high, exceeding ~10 MW/cm^2, which is caused by "gain switching" in the cavity at a very low initial radiation field in the cavity. At these operating conditions, approximately 25% of the total vibrational energy flux, or ~ 500 W, is coupled out as laser power. Thus, the model predicts that a very powerful c.w. laser is possible at these operating conditions.

While modeling calculations suggest the proposed laser system will be successful, much experimental validation is required. The major issue addressed in this study is the predicted production of extremely high power loading of the CO vibrational mode, and the persistence of strong lasing even at temperatures well in excess of the low, near cryogenic values (~125 K) of the most powerful and efficient electrically-excited CO lasers. Lasing tests in high power loading conditions, together with detailed measurements of vibrational state populations and lasing output, provide a data basis to test the validity of the modeling codes used in the analysis of the supersonic flow laser.

3.3. Optically Pumped CO Laser Experiments and Kinetic Model Validation

For the validation measurements, experiments were conducted in a flowing gas cell, in which CO in an Ar diluent was vibrationally-excited by absorption of powerful radiation coming from two electrically-excited CO lasers. This experimental setup is shown in Fig. 21. In the middle of the figure is the flowing gas absorption cell. Top and bottom are the two CO lasers (Pump laser A and Pump laser B). The optical arrangement is such that the absorption cell and both pump lasers are within a single optical cavity. Two pump lasers are used to insure maximum power delivery to the flowing CO in the absorption cell. The cell is equipped with optical windows along its length, to enable spontaneous radiation from the vibrationally excited CO in the cell to be monitored by Fourier Transform Infrared (FTIR) emission spectroscopy,

using the Bruker instrument shown. From analysis of these emission spectra, the distribution of populations of the vibrational quantum states and the translational/rotational mode temperature in the pumped cell are inferred. Further, the cell is equipped with a dichroic mirror and a total reflector, as shown, which establish a laser cavity for the cell alone, and any CO laser radiation arising from the cell is monitored on the Varian FTIR spectrometer shown. Mixtures of a few percent of CO in Ar flow through the cell at velocities in the range of 5 to 25 cm/sec. The in-cavity radiation generated by the pump lasers is of O[1 kW c.w.]. With this level of pump intensity, the CO in the cell absorbs considerable power in the vibrational states, with power loadings above those typical of conventional CO lasers. Full details of these experiments are given in Ref. [42]; here, we summarize some key results.

Fig. 22 shows CO vibrational distribution functions inferred from the emission spectra radiated from the central side window in the cell, when the pump laser fields are on, maintaining high levels of vibration excitation in the flowing CO. As in the previous model calculations we have shown, the relative populations of each vibrational state, normalized by the ground state population, N_v/N_0, is plotted against vibrational quantum number. Here, however, the circular symbols show actual experimental measurement of each state population. Two such experimental distributions are shown. The distribution with the larger state populations is when the resonator mirrors on the cell are unaligned; no laser power is being removed. The distribution with the smaller state populations is when the resonator mirrors on the cell are aligned, and substantial laser power is being removed from the cell. The lowered populations of the vibrationally excited states are striking. The two line distributions shown in the figure are the kinetic model calculations, done for the experimental conditions of the data, i.e., cell resonator aligned and lasing, and cell unaligned and no lasing power being removed. The excellent agreement with the predictions of the model in both cases is evident; it must be emphasized that there are no adjustable parameters in the model; all inputs are actual kinetic rate data, theory, and known absorption and radiative emission coefficients.

Further validation of the predictive model was afforded by studies of the working laser resonator established on the pumped cell. Fig. 23 shows such a prediction for the cell resonator. In this case, a 3% mixture of CO in Ar is flowing through the cell, at a pressure of 10 Torr and 335 K temperature. Just under 10 W of power from one pump laser is entering the cell. The figure shows the actual measured power spectrum entering the cell from the pump laser, on the left in blue. The pump laser lines range from those from the $v = 2 \rightarrow 1$ vibrational band component to those from the $v = 8 \rightarrow 7$ band component. The rotational quantum numbers of these vib-rot lines are indicated by the blue triangles, and the rotational quantum numbers of the upper laser state are referred to the scale on the right hand side of the plot. For these pump conditions, the prediction of the modeling code for the cell resonator laser output is given in red. It is assumed that the total gain length established on the cell by its mirrors is 100 cm. The predicted output power spectrum from the cell resonator is shown in the red vertical bars, and the corresponding rotational quantum numbers of these vibrational-rotational lines are indicated by the red circles. Note that the pump laser spectrum is from lower vibrational state transitions, and rotational quantum levels of these pump laser lines are in the range J = 7 to J = 11. Such values are typical for the electrically-excited, liquid nitrogen wall cooled CO laser used for the pump, where the average temperature of the laser gases is ~150 K. On the other hand, the pumped cell is much warmer (335 K), and the predicted laser output arises from considerably higher, more populated rotational states in the range J = 16 to J =20. In addition, the model predicts that most of the pump laser radiation will be absorbed, and the cell will lase higher

vibrational band components, extending from v = 9 → 8 to v = 23 → 22, as shown. The predicted conversion efficiency for this case is 28%, i.e., 2.8 W of the input pump excitation power of 10 W is produced at output from the cell resonator.

Fig. 24 shows the actual performance of the pumped cell resonator for the conditions of the model predictions of Fig. 22. The lower spectrum of the figure shows the remaining power spectrum in cavity with the cell resonator is unaligned, but with CO flowing in the cell. This can be compared with the totally unabsorbed power spectrum coming from the pump laser in Fig. 23. It can be seen that some of the pump laser lines are totally absorbed by the cell, and others are diminished. The upper spectrum is the laser power spectrum coming from the cell with the cell resonator aligned. Lines that appear in the pump radiation are shown in blue, and the additional lines generated only in the optically pumped cell are shown in red. The agreement with the model predictions is excellent. As predicted, the cell is lasing on higher vibrational band components, and on rotational levels reflecting the high cell temperature. The actual band component and vibrational-rotational line assignments are given on the figure. We note that the actual gain path is shorter than the 100 cm assumed for the model calculation, and actual cavity losses are somewhat greater than those assumed in the calculations. This performance is consistent with the lower reflectivity of the resonator mirrors at the shorter wavelengths, shown on the black curve. Again, consistent with the model calculations and the shorter experimental gain length, actual conversion efficiency by the cell is as high as 14.4 %, and the cell lases at temperatures as high as 415 K.

We conclude that this validates the kinetic model used for a major nonequilibrium flow system.

4. Conclusions

High enthalpy flows that have substantial amounts of thermodynamic disequilibrium in internal energy modes have long offered substantial challenges to engineers seeking methods for analysis and design. In modeling, the usual descriptive equations of continuum fluid mechanics must be supplemented by kinetic equations governing the energy transfer among energy modes and chemical reactions governing species concentrations. The rates of such processes must be measured or predicted theoretically for incorporation into the kinetic equations. Most critically, validation of the descriptive equations can only be accomplished by detailed experimental measurement in the flow. It is necessary to measure the energy content in each mode, the species densities, and, often, the specific quantum state populations in each mode. Measurement, particularly in hypersonic/supersonic flow fields, must be non-intrusive, and often there is an additional requirement for high spatial- and time- resolution of such measurements.

As reviewed in the present chapter, there has been some substantial recent progress in addressing these challenges. Optical emission measurements, and laser-based spectroscopic interrogation diagnostics, play a major role in experimental studies of the flows. It is possible to resolve state populations and rotational mode temperatures in the layer behind a bow shock in the small tunnel studied. We emphasize that these non-intrusive laser diagnostic systems are complex, and development has depended on use of a small tunnel with relatively long run times and short turn around periods. This development must be done before transferring the diagnostic to larger scale, short-test-time facilities. Similar considerations pertain to the development of a

new high power flowing gas laser system, as reviewed above. Experiments and modeling of a laboratory-scale system is essential before development of a large scale device. In summary, the approaches reviewed here afford means for extensive future development of vital nonequilibrium flow devices.

5. Acknowledgements

We gratefully acknowledge the support of: The Air Force Office of Scientific Research for basic studies of nonequilibrium hypersonic flows (Program Manager Dr. John Schmisseur); The Lockheed Martin Corporation for hypersonic flow laser energy recovery studies (Program Managers Drs. Luke Uribarri and Ned Allen); and The Michael A. Chaszeyka Gift to the OSU Nonequilibrium Thermodynamics Laboratories. We wish to thank Dr. Graham Candler and his co-workers for CFD Navier –Stokes modeling calculations of the M = 5 wind tunnel, and Drs. George Schatz and Timothy Minton for sharing their results for creating population inversions in CO, prior to publication.

References

1. M. Nishihara, K. Takashima, N. Jiang, W.R. Lempert, I.V. Adamovich, J.W. Rich, S. Doraiswamy, and G.V. Candler, “Development of a Mach 5 Nonequilibrium Flow Wind Tunnel”, AIAA Journal, vol. 50, 2012, pp. 2255-2267
2. M. Nishihara, N. Jiang, J.W. Rich, W.R. Lempert, I.V. Adamovich, and S. Gogineni, “Low-Temperature Supersonic Boundary Layer Control Using Repetitively Pulsed MHD Forcing”, Physics of Fluids, vol. 17, No. 10, 2005, p. 106102
3. M. Nishihara, J.W. Rich, W.R. Lempert, I.V. Adamovich, and S. Gogineni, “Low-Temperature M=3 Flow Deceleration by Lorentz Force”, Physics of Fluids, vol. 18, No. 8, 2006, p. 086101
4. J.R. Bruzzese, A. Hicks, A. Erofeev, A.C. Cole, M. Nishihara, and I.V. Adamovich, "Gain and Output Power Measurements in an Electrically Excited Oxygen-Iodine Laser with a Scaled Discharge", Journal of Physics D: Applied Physics, vol. 43, 2010, p. 015201
5. Raizer, Yu.P., "Gas Discharge Physics", Springer-Verlag, Berlin, 1991
6. Chatelet, M., and Chesnoy, J., “New Results on the Vibrational Relaxation Time in Compressed Nitrogen at 293 K”, Chemical Physics Letters, vol. 122, 1985, p. 550-552
7. A. Montello, M. Nishihara, J.W. Rich, I.V. Adamovich, and W.R. Lempert, “Picosecond CARS Measurements of Nitrogen Rotational/ Translational and Vibrational Temperature in a Nonequilibrium Mach 5 Flow”, Experiments in Fluids, vol. 54, 2013, 1422
8. M. Nishihara, K. Udagawa Takashima, J.R. Bruzzese, I.V. Adamovich, and D. Gaitonde, “Experimental and Computational Studies of Low-Temperature Mach 4 Flow Control by Lorentz Force”, Journal of Propulsion and Power, vol. 27, 2011, pp. 467-476
9. Nompelis, I., Drayna, T.W., and Candler, G.V., “Development of Hybrid Unstructured Implicit Solver for the Simulation of Reacting Flows Over Complex Geometries,” AIAA Paper 2004–2227, 34th AIAA Fluid Dynamics Conference and Exhibit, Portland, Oregon, June 28-1, 2004
10. Nompelis, I., Drayna, T.W., and Candler, G.V., “A Parallel Unstructured Implicit Solver for Hypersonic Reacting Flow Simulations,” AIAA Paper 2005–4867, 17th AIAA Computational Fluid Dynamics Conference, Toronto, Ontario, June 6-9, 2005
11. Candler, G.V., “Hypersonic Nozzle Analysis Using an Excluded Volume Equation of State,” AIAA Paper 2005–5202, 38th AIAA Thermophysics Conference, Toronto, Ontario, June 6-9, 2005
12. Thurow, B., Jiang, N., Samimy, M., and Lempert, W., “Narrow-Linewidth Megahertz-Rate Pulse-Burst Laser for High-Speed Flow Diagnostics,” Applied Optics, vol. 43, 2004, pp. 5064-5073
13. Jiang, N., Webster, M., and Lempert, W.R., “New Advances in Generation of High Repetition Rate Burst Mode Laser Output,” Applied Optics, vol. 48, 2009, pp. B23-B31
14. Jiang, N., and Lempert, W.R., “Ultra-High Frame Rate Nitric Oxide Planar Laser Induced Fluorescence imaging,” Optics Letters, vol. 33, 2008, pp. 2236-2238
15. Eckbreth, A.C., “Laser Diagnostics for Combustion Temperature and Species,” Amsterdam, Gordon and Breach, 1996

16. Roy, S., Gord, J.R., Patnaik, A.K., “Recent Advances in Coherent Anti-Stokes Raman Scattering Spectroscopy: Fundamental Developments and Applications in Reacting Flows,” Progress in Energy and Combustion Science, vol. 36, 2010, p. 280-306
17. Marko, K.A. and Rimai, L., “Space- and Time-Resolved Coherent Anti-Stokes Raman Spectroscopy for Combustion Diagnostics,” Optics Letters, vol. 4, no. 7, 1979, p. 211
18. Klick, D., Marko, K.A., and Rimai, L., “Broadband Single-Pulse CARS spectra in a Fired Internal Combustion Engine,” Applied Optics, vol. 20 no. 7, 1981, p. 1178
19. Roy, S., Meyer, T.R., and Gord J.R., “Broadband Coherent Anti-stokes Raman Scattering Spectroscopy of Nitrogen Using a Picosecond Modeless Dye Laser”, Optics Letters, vol. 3, 2005, p. 3222
20. Montello, A., Nishihara, M., Rich, J.W., Adamovich, I.V., and Lempert, W.R, “Nitrogen Vibrational Population Measurements in the Plenum of a Hypersonic Wind Tunnel," AIAA Journal, vol. 50, 2012, p. 1367
21. Guerra V, Sa PA, Loureiro J, “Role Played by the $N_2(A^3\Sigma_g^+)$ Metastable in Stationary N_2 and $N_2 – O_2$ Discharges”, Journal of Physics D: Applied Physics, vol. 34, 2001, pp. 1745-1755
22. Palmer, R.E., “The CARSFT Computer Code for Calculating Coherent Anti-Stokes Raman Spectra: User and Programmer Information,” Sandia National Labs., Rept. SAND89-8206, Livermore, CA, 1989.
23. Taylor, R.L., and Bitterman, S., “Survey of Vibrational Relaxation Data for Processes Important in the CO_2-N_2 laser System,” Reviews of Modern Physics, vol. 41, 1969, pp. 26-47
24. Doyennette, L., and Margottin-Maclou, M., “Vibrational relaxation of NO(v=1) by NO, N2, CO, HCl, CO2, and N2O from 300 to 600 K,” Journal of Chemical Physics, vol. 84, 1986, pp. 6668-6678
25. Allen, D.C., Chandler, E.T., Gregory, E.A., Siddles, R.M., and Simpson, C.J.S.M., “Vibrational deactiviation of N_2 (v=1) by n-H_2 and by p-H_2,” Chemical Physics Letters, vol. 76, 1980, pp. 347-353
26. Capitelli, M., Ferreira, C.M., Gordiets, B.F., and Osipov, A.I., “Plasma Kinetics in Atmospheric Gases”, Springer, Berlin, 2001, Chap. 7
27. Bott, J.F., “Vibrational Energy Exchange between H_2(v=1) and D_2, N_2, HCl, and CO_2,” J. Chem. Phys., vol. 65, 1976, pp. 3921-3928
28. Ahn, T., Adamovich, I.V., and Lempert, W.R., “Determination of Nitrogen V-V Transfer Rates by Stimulated Raman Pumping,” Chemical Physics, vol. 298, 2004, pp. 233-240
29. Kim, C.-S., “Experimental Studies of Supersonic Flow past a Circular Cylinder,” Journal of the Physical Society of Japan, vol. 11, 1956, pp. 439-445
30. G.M. Grigor’yan, B.M. Dymshits, S.V. Izyumov, Sov. J. Quant. Electron. 17, 1385, 1987
31. Dymshitz, B.M., et al., “CW 200 kW Supersonic CO Laser”, Proc. SPIE, vol. 2206, 1994, p. 109
32. Bergman, R.C., and Rich, J.W., “Overtone Bands Lasing at 2.7 – 3.1 μm in Electrically Excited CO”, Applied Physics Letters, vol. 31, 1977, p. 597
33. Y.G. Utkin, M. Goshe, I.V. Adamovich, and J.W. Rich, “Compact High Overtone Band Carbon Monoxide Laser”, Optics Communications, vol. 263, 2006, pp. 105-110

34. A. Ionin, “Electric Discharge CO Lasers”, in “Gas Lasers”, Ed. By E. Masomori and R.F. Walter, Chapter 5, pp. 201-238, CRC Press, Boca Raton, FL, 2007
35. Rich, J.W., “Kinetic Modeling of the High-Power Carbon Monoxide Laser”, Journal of Applied Physics, vol. 42, 1971, p. 2719
36. Treanor, C.E., Rich, J.W., and Rehm, R.G., “Vibrational Relaxation of Anharmonic Oscillators with Exchange-Dominated Collisions”, Journal of Chemical Physics, vol. 48, 1968, p. 1798
37. Lin, M.C., Umstead, M.E., and Djeu, N, “Chemical Lasers”, Annual Reviews of Physical Chemistry, vol. 34, 1983, pp. 557-591
38. Schatz, G., Private Communication, 2012
39. Minton, T, Private Communication, 2013
40. E. Ploenjes, P. Palm, A.P. Chernukho, I.V. Adamovich, and J.W. Rich, “Time-Resolved Fourier Transform Infrared Spectroscopy of Optically Pumped Carbon Monoxide”, Chemical Physics, vol. 256, 2000, pp. 315-331
41. S.D. Rockwood, J.E. Brau, W.A. Proctor, and G.H. Canavan, “Time-Dependent Calculations of Carbon Monoxide Laser Kinetics”, IEEE Journal of Quantum Electronics, vol. 9, 1973, pp. 120-129
42. E. Ivanov, K. Frederickson, S. Leonov, W.R. Lempert, I.V Adamovich, and J.W. Rich, “Optically Pumped Carbon Monoxide Laser Operating at Elevated Temperatures”, Laser Physics, vol. 23, 2013, p. 095004
43. Hsu, D.S.Y., Shaub, W.M., Burks, T.L., and Lin, M.C., Chemical Physics, vol. 44, 1979, pp. 143-150
44. Hancock, G., Ridley, B.A., Smith, I.W.M., J. Chem. Soc. Faraday Trans. 2, vol. 68, 1972, pp. 2117-26
45. Djeu, N., J. Chem. Phys., vol. 60, 1974, pp. 4109-15

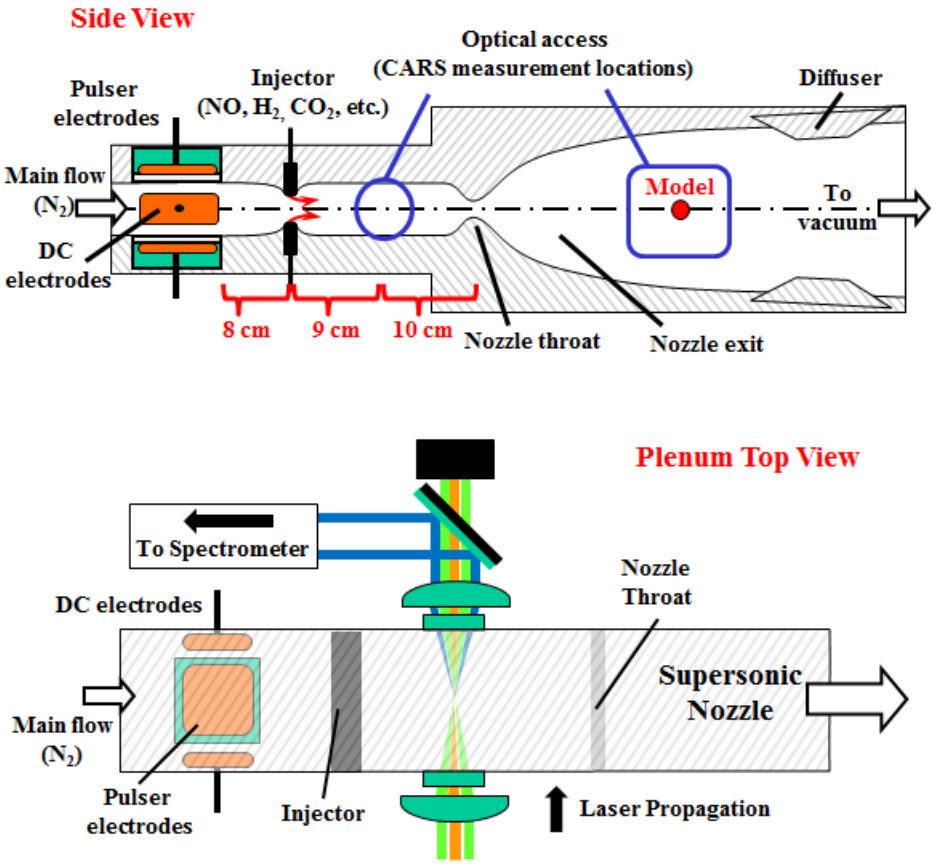

Figure 1. Schematic of the Mach 5 nonequilibrium plasma wind tunnel.

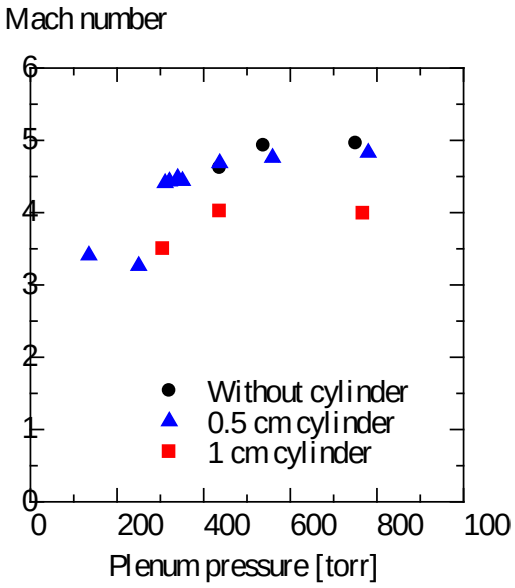

Figure 2. Test section Mach number vs. plenum pressure, inferred from the static pressure measured at the end of the nozzle. At P_0=760±0.05 torr, baseline test section static pressure is P=1.5±0.05 torr.

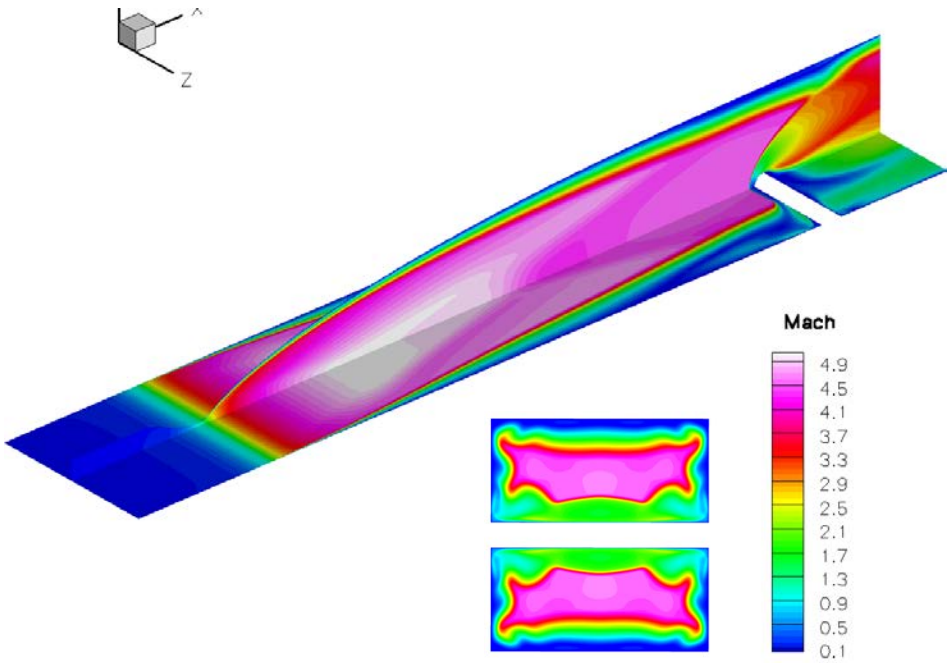

Figure 3. Mach number distributions in the entire wind tunnel (top) and in the flow cross section through the cylinder model axis (bottom), predicted by a 3-D compressible Navier-Stokes CFD flow code. Nitrogen, T_0=300 K, P_0=380 torr.

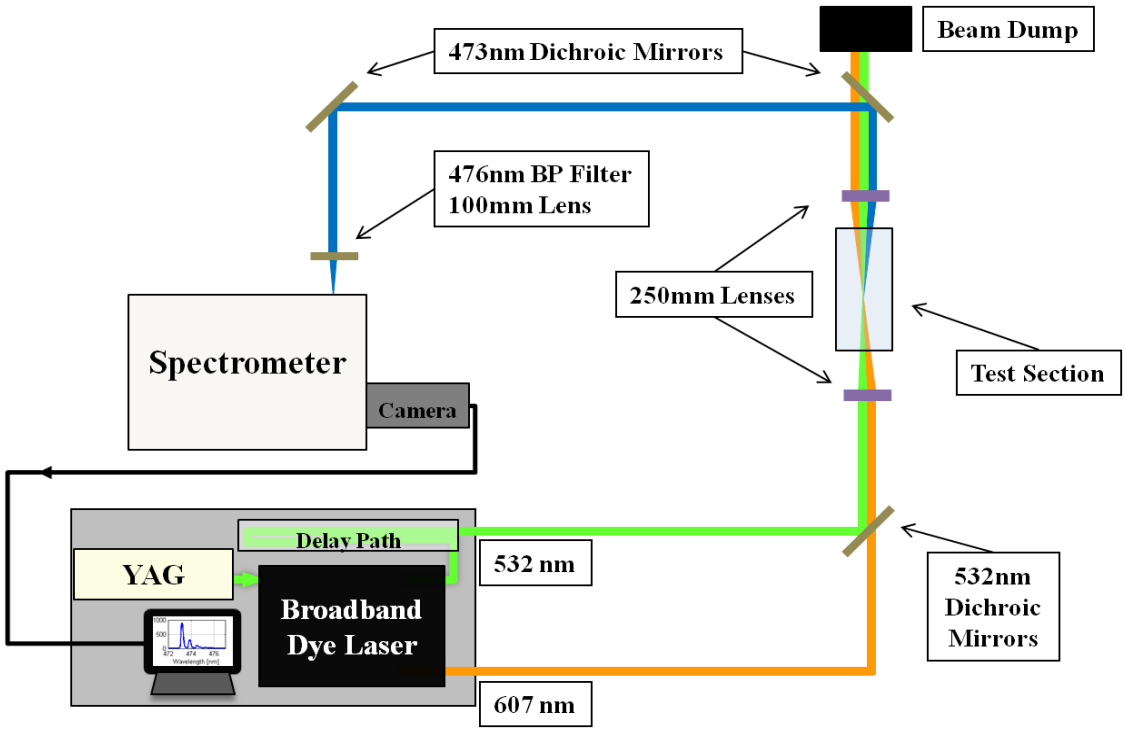

Figure 4. Schematic diagram of psec CARS system.

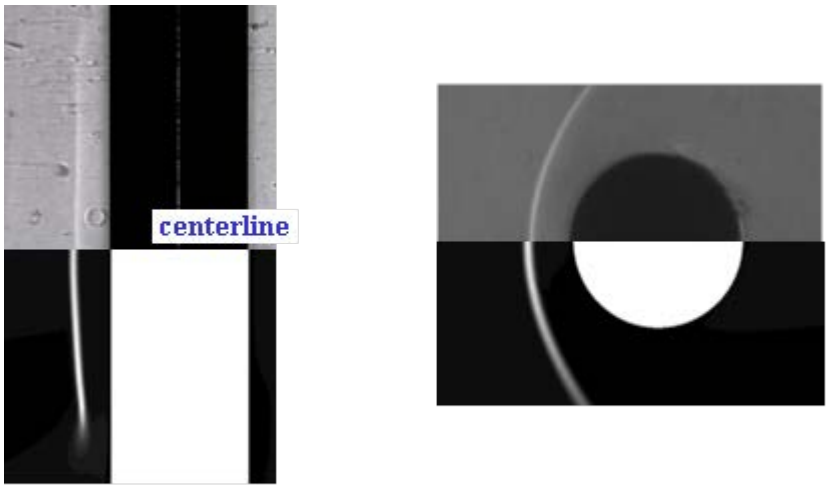

Figure 5. Comparison of experimental (top) and CFD (bottom) schlieren images of a bow shock in front of a 5 mm diameter cylinder in the supersonic test section (top view and side view). Nitrogen, P_0=350 torr, cold flow (no plasma). Shock stand-off distance 1.2 mm.

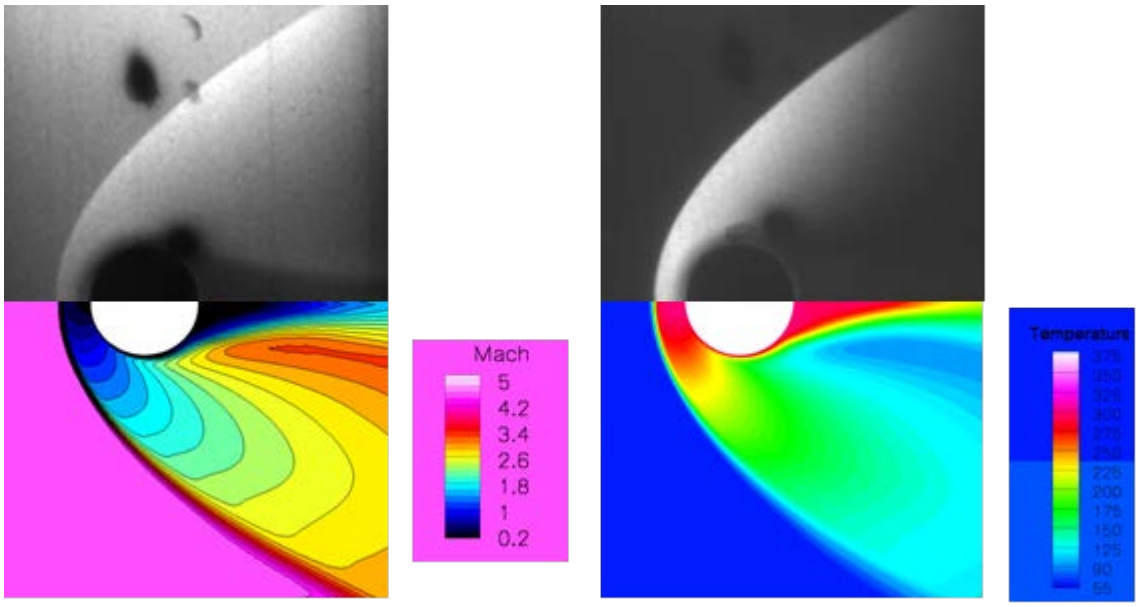

Figure 6. Left: comparison of a broadband NO PLIF image of Fig. 18(a) with 3-D compressible flow CFD calculations showing Mach number distribution. Right: comparison of a single-line NO PLIF image of Fig. 18(b) with 3-D compressible flow CFD calculations showing temperature field. Nitrogen, P_0=350 torr, cold flow (no discharge).

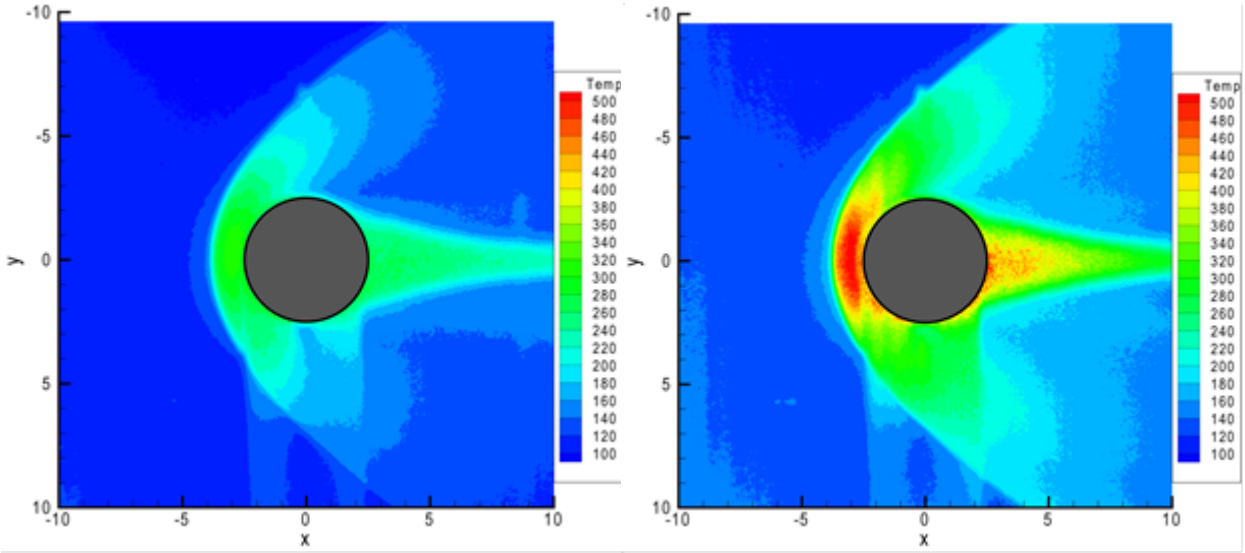

Figure 7. Rotational temperature distributions inferred from NO PLIF images. Left: cold flow, temperature at stagnation point T=300±30 K. Right: flow excited by a pulser sustainer discharge (ν=100 kHz, U_{PS}=4.5 kV), temperature at stagnation point T=500±190 K. Nitrogen, P_0=370 torr, NO mole fraction 0.3%.

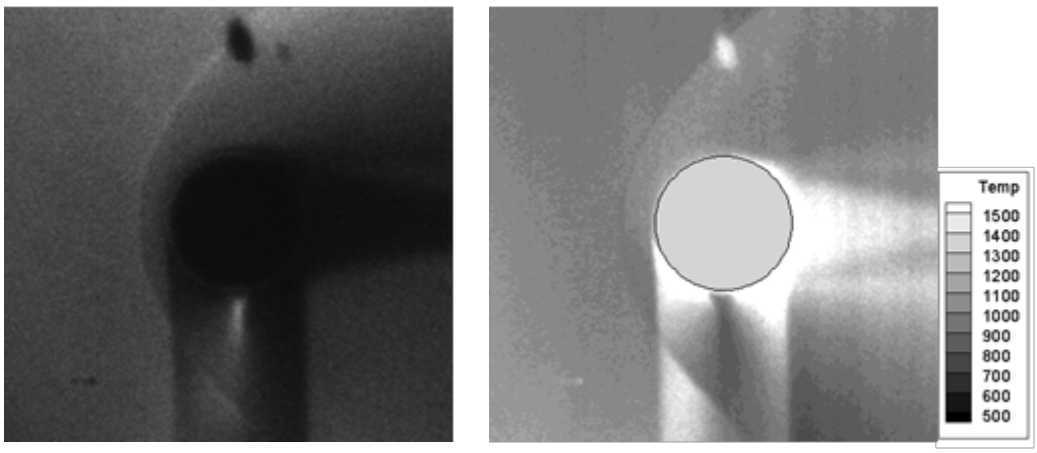

Figure 8(a,b). Left: NO(v=1) PLIF image of a flow in the supersonic test section. Nitrogen, P0=350 torr, NO mole fraction 0.3%, excited by a pulsed/DC discharge (ν=100 kHz, UPS=4.5 kV). Laser operated on a NO(X,v″=1→A,v′=1), Q_{11}+P_{21} (J=3.5) line, pulse repetition rate 10 Hz, 10 pulses/burst, image integrated over 10 pulses (1 msec). Right: vibrational temperature distribution inferred from PLIF images. Free stream NO vibrational temperature T_v(NO) = 1,000 ± 170 K.

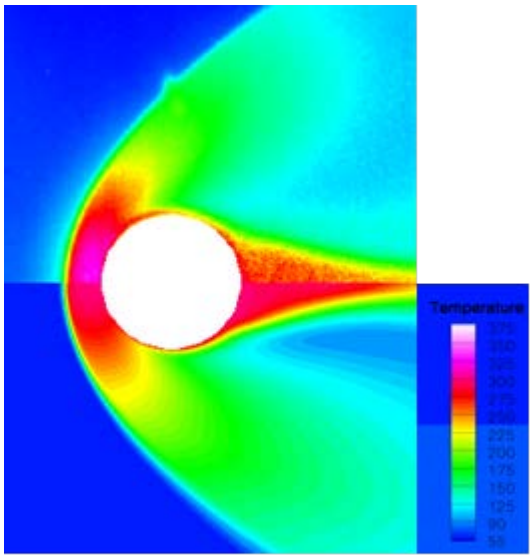

Figure 9. Comparison of experimental (top) and CFD (bottom) temperature distributions for cold flow conditions (nitrogen, P_0=370 torr, T_0=300 K).

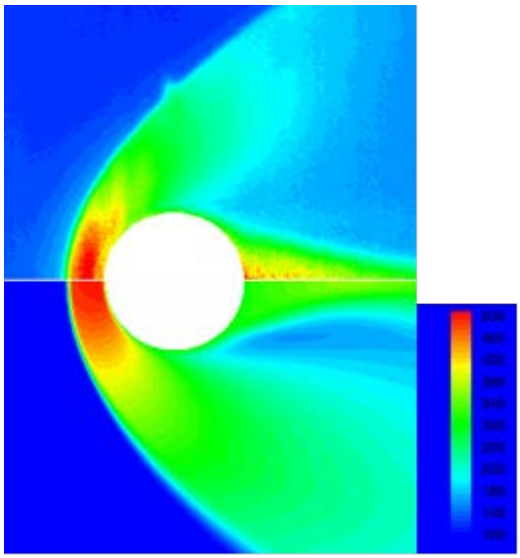

Figure 10. Comparison of experimental (top) and CFD (bottom) temperature distributions with a with a pulsed/DC discharge operating in plenum (ν=100 kHz, U_{PS}=4.5 kV). Nitrogen, P_0=370 torr. In the calculations, plenum conditions are T_0=500 K, T_{v0}=1700 K.

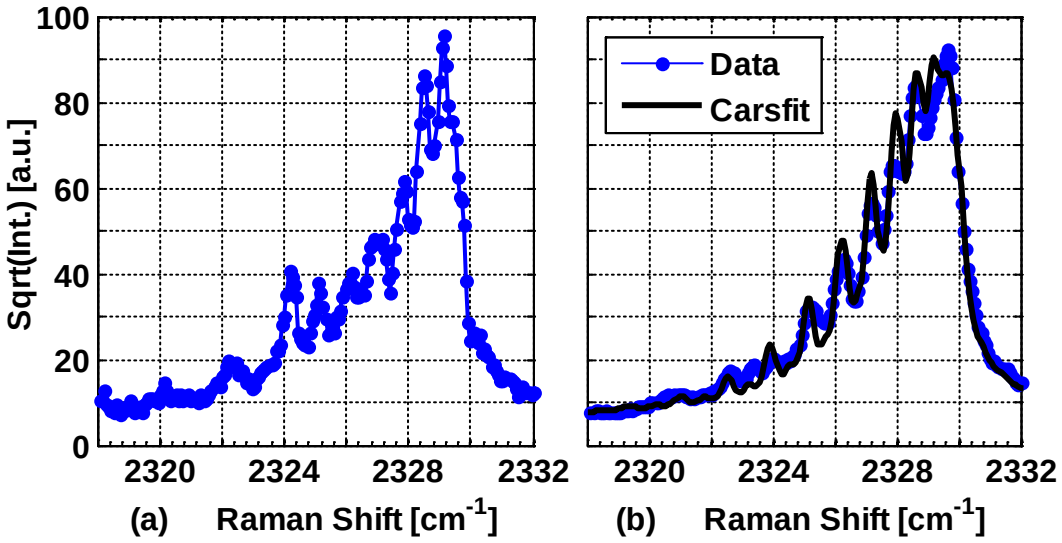

Figure 11. Pure N_2 CARS spectra at 370 torr with no discharge, (a) single-shot and (b) 20-shot average, along with Carsfit best synthetic spectra; T_{fit} = 322 K.

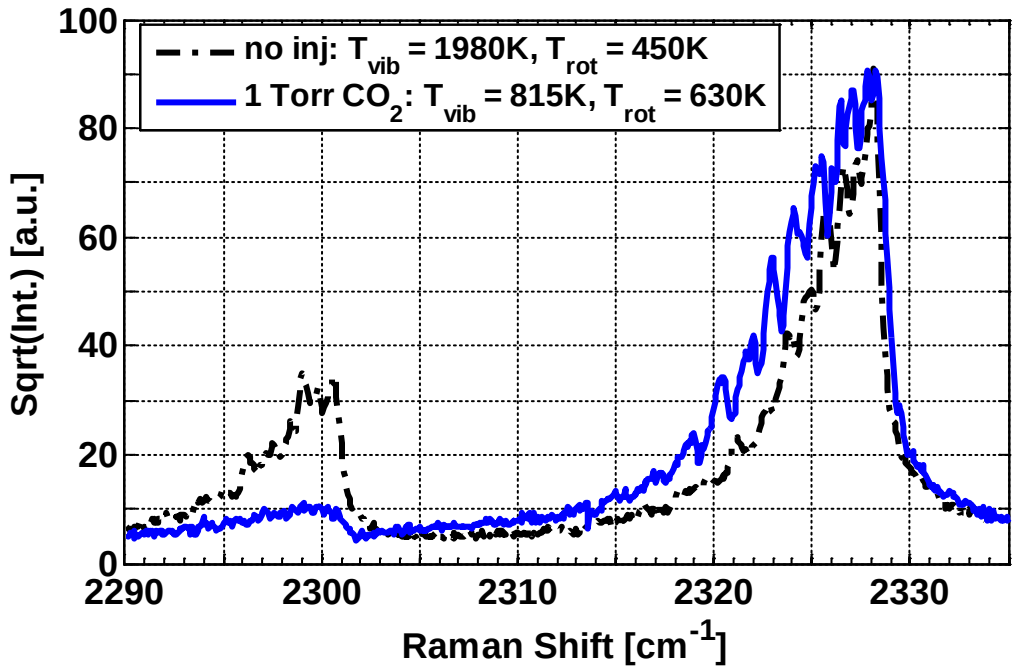

Figure 12. CARS spectra for pulser-sustainer discharge at 300 torr total pressure, in pure nitrogen (i.e. no relaxer injection, black dash-dot) and 1 torr CO_2 partial pressure injection (blue solid).

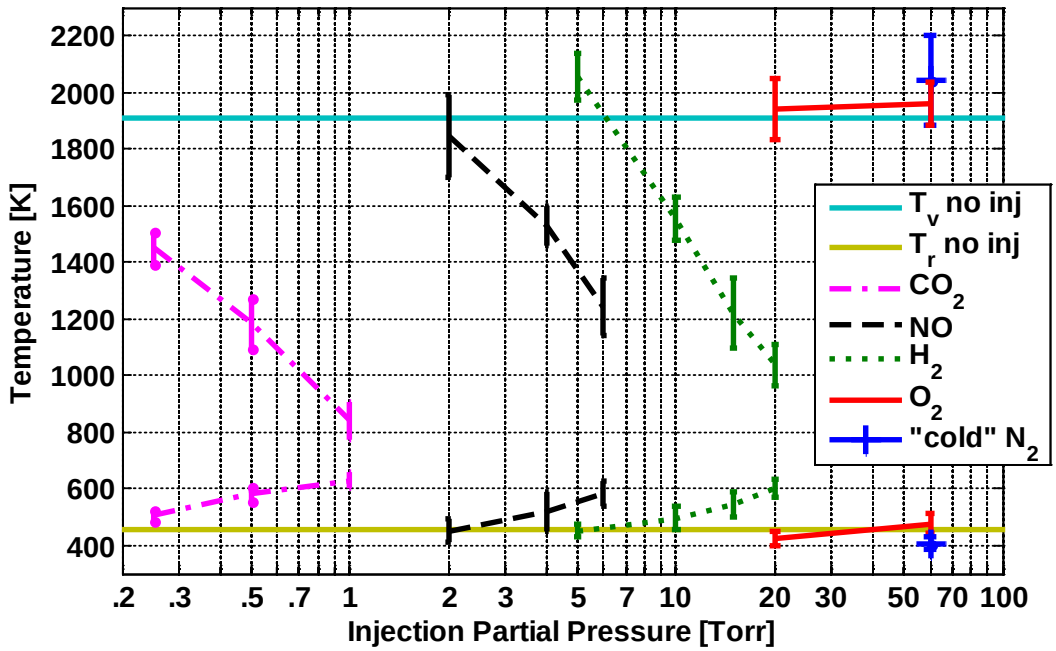

Figure 13. Pulser-sustainer discharge, V_{PS} = 4.5 kV, various injected species, 300 torr total mixture pressure.

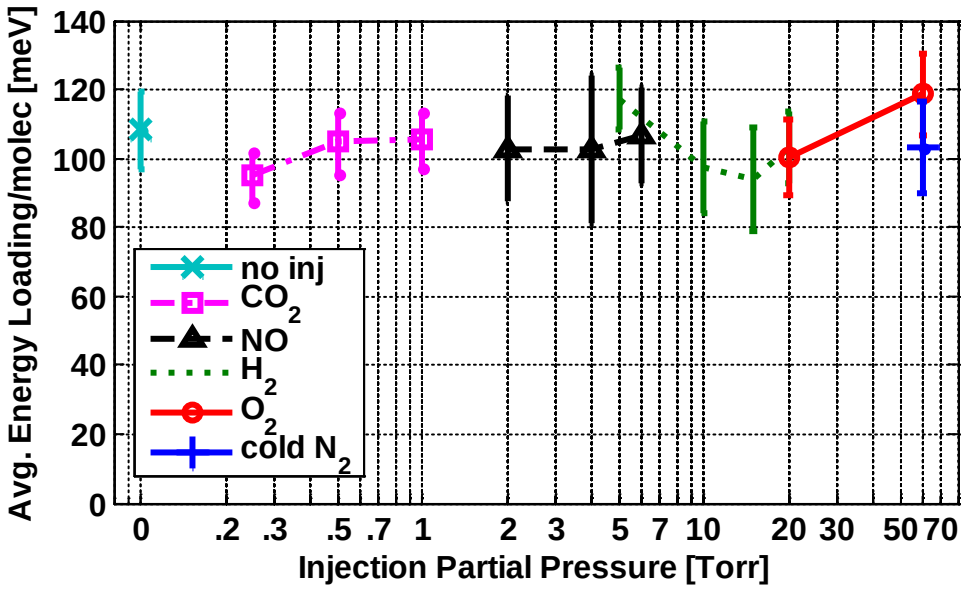

Figure 14. Sum of nitrogen translational + rotational + vibrational energy as a function of relaxant species partial pressure.

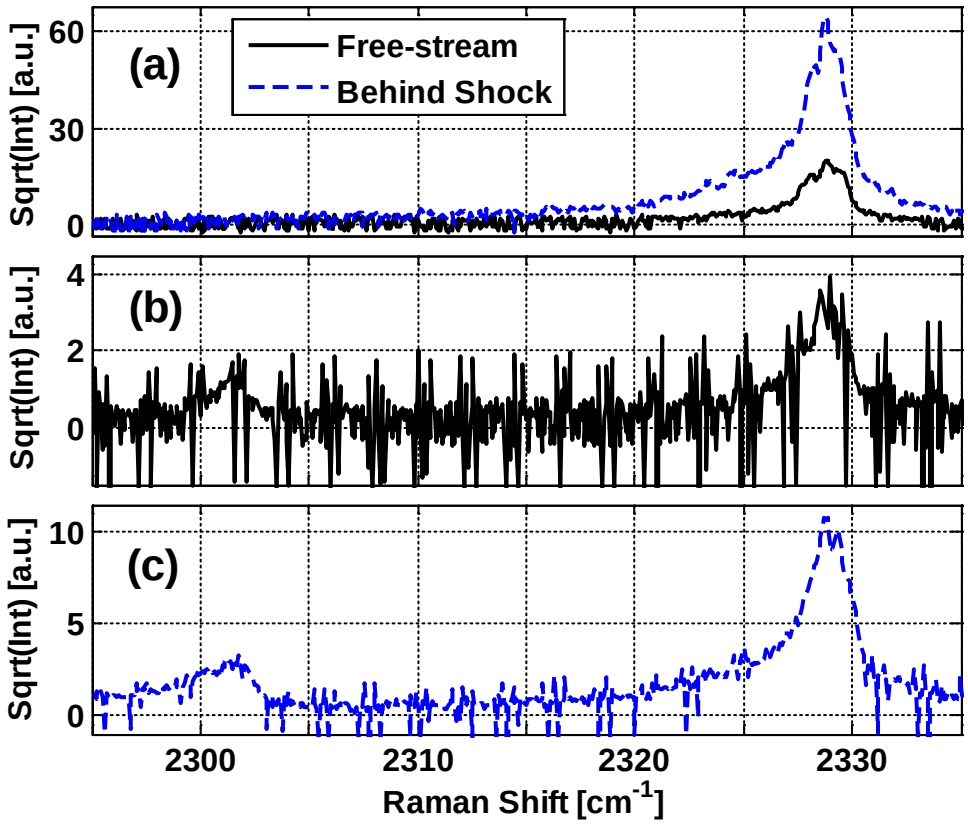

Figure 15. Sample CARS spectra collected in the supersonic flow; (a) eight-shot average spectra collected in the free-stream and behind the shock layer with no discharge present; ten-shot average spectra with the pulser-sustainer discharge operating, collected in the (b) supersonic free-stream and (c) behind the bow shock.

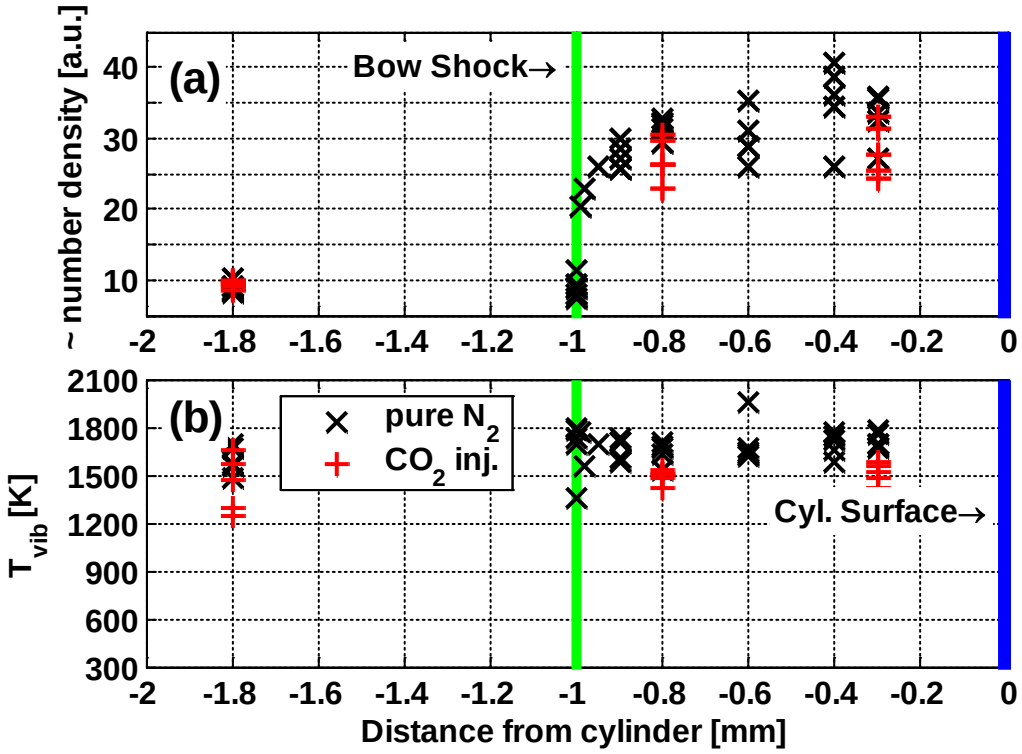

Figure 16. Inferred (a) estimated number density, and (b) vibrational temperature in the supersonic flow free-stream and behind the bow shock.

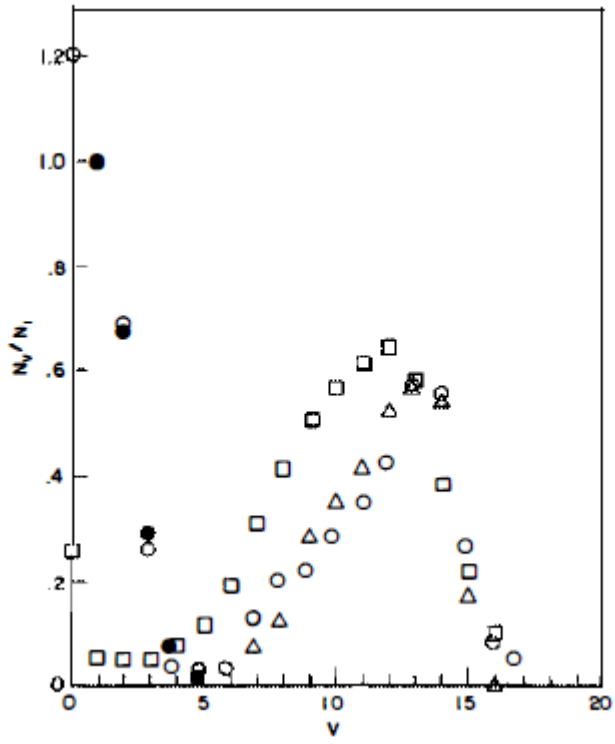

Figure 17. Relative CO vibrational energy distribution from the O(^{3}P) + CSand CS_2 reactions. Distributions obtained by Hsu et al. [43] for the O + CS_2 reaction (filled circles) and the O + CS reaction (open circles), both normalized to v = 1. Data obtained from the O + CS reaction by Hancock et al. [44] (triangles) and by Djeu [45] (squares), both normalized to v = 13 of the open circle distribution. The distributions below v = 5 are attributable to the O + CS_2 reaction.

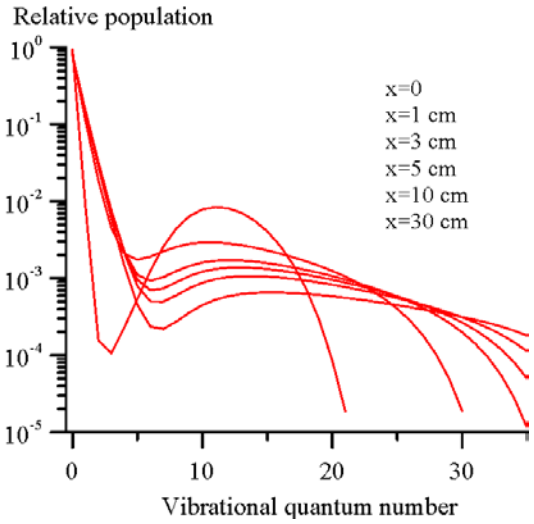

Figure 18. CO vibrational state populations predicted by the model, shown at several locations downstream from the throat, without laser mirrors in the cavity.

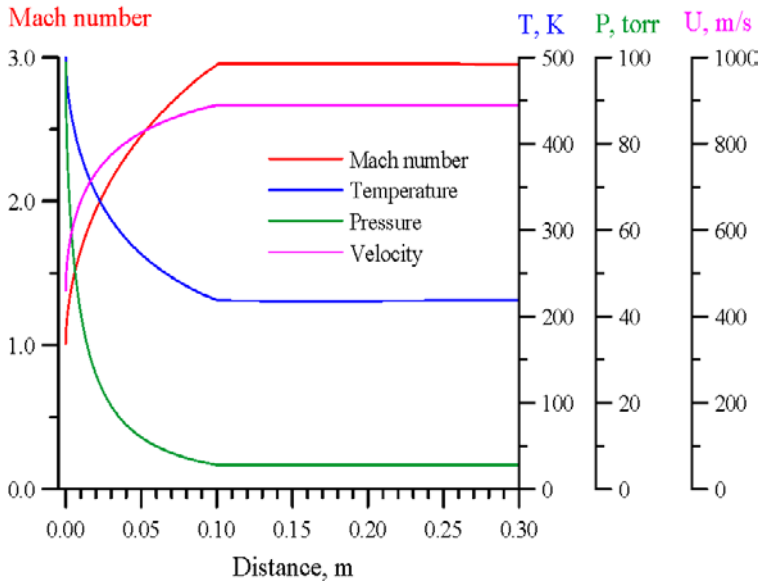

Figure 19. Calculated flow parameters along the laser nozzle, without laser mirrors in the cavity.

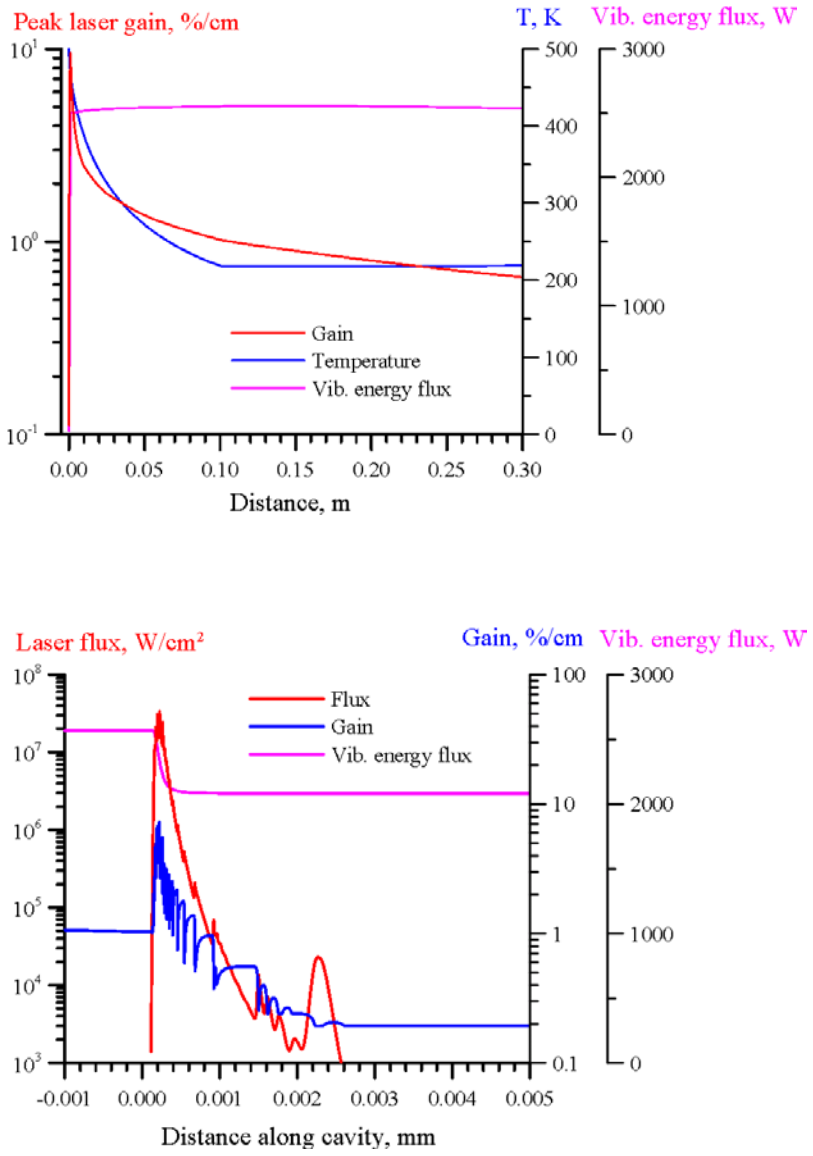

Figure 20. Calculated laser parameters along the laser nozzle, (a) without laser mirrors, and (b) with mirrors in the cavity.

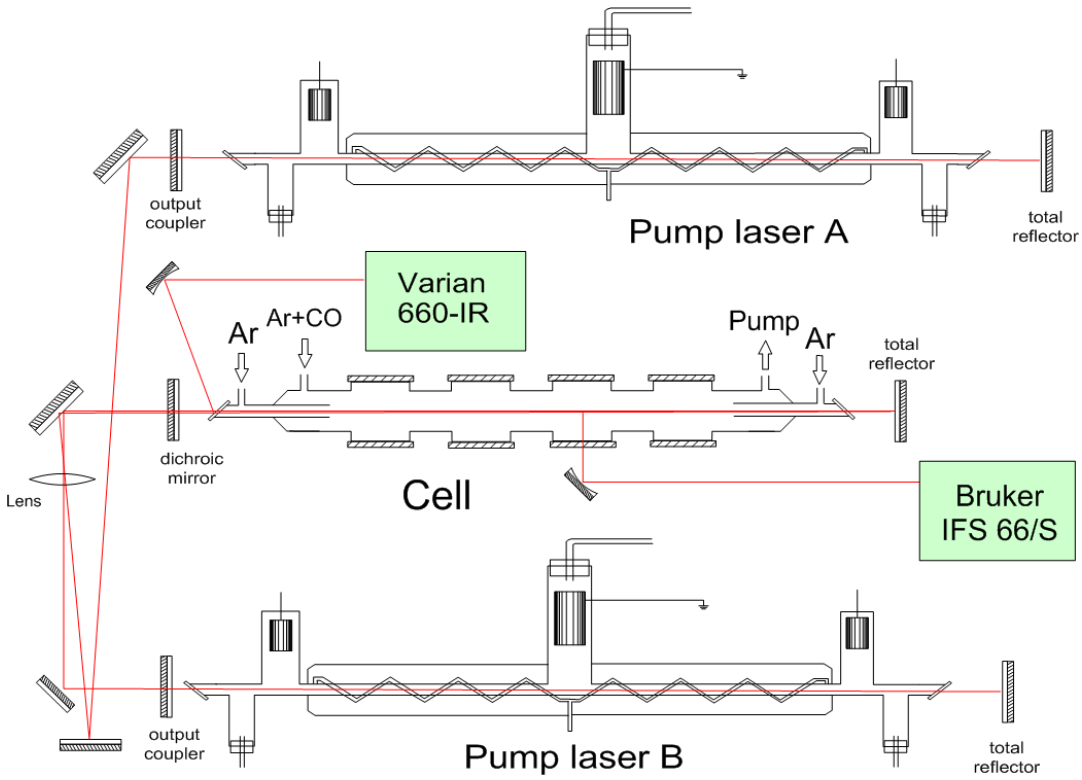

Figure 21. Experimental setup for high energy loading of the CO vibrational mode.

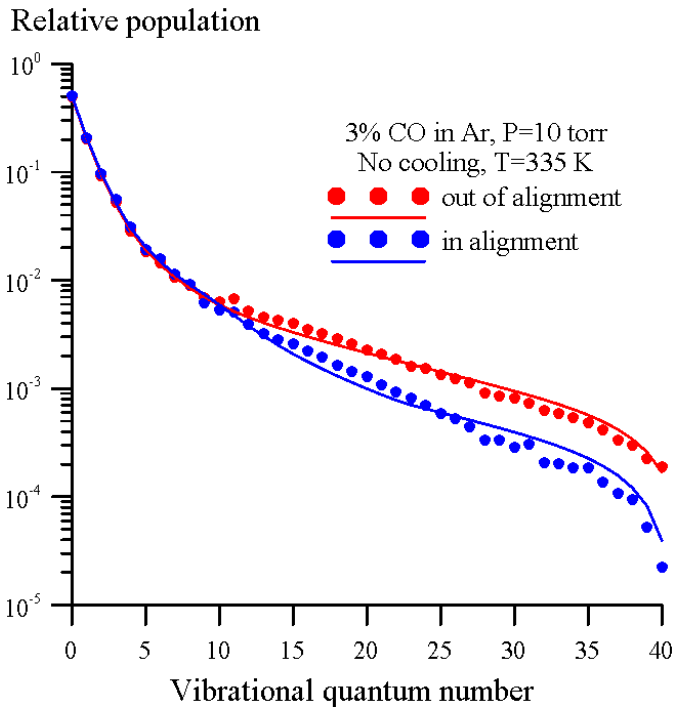

Figure 22. Experimental measurement and model prediction of vibrational population distributions in an optically pumped cell. Symbols: CO vibrational distribution functions inferred from the emission spectra, with the resonator in and out of alignment. Lines: kinetic model predictions at the same conditions. Reduction of high CO vibrational level populations, caused by stimulated emission energy removal in the cell during lasing (when resonator is aligned), is apparent.

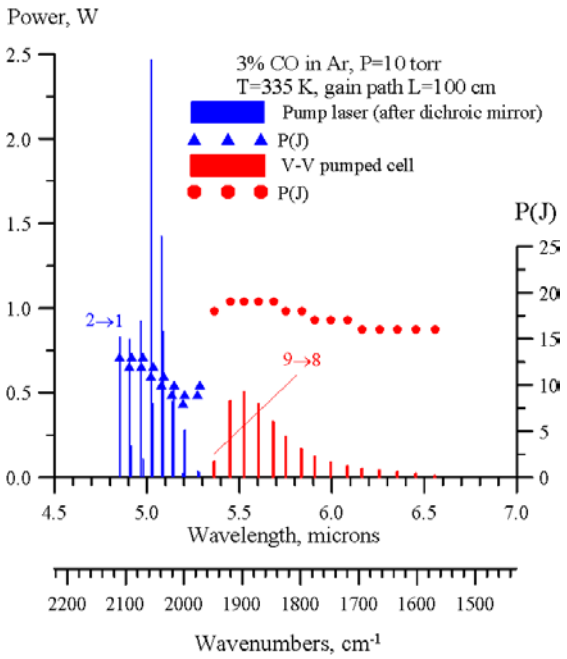

Figure 23. Pump CO laser spectrum (blue) measured after the dichroic mirror (9.4 W) and optically pumped laser spectrum (red) predicted by the model at the conditions of Fig. 22 (resonator in alignment). Predicted conversion efficiency 28%.

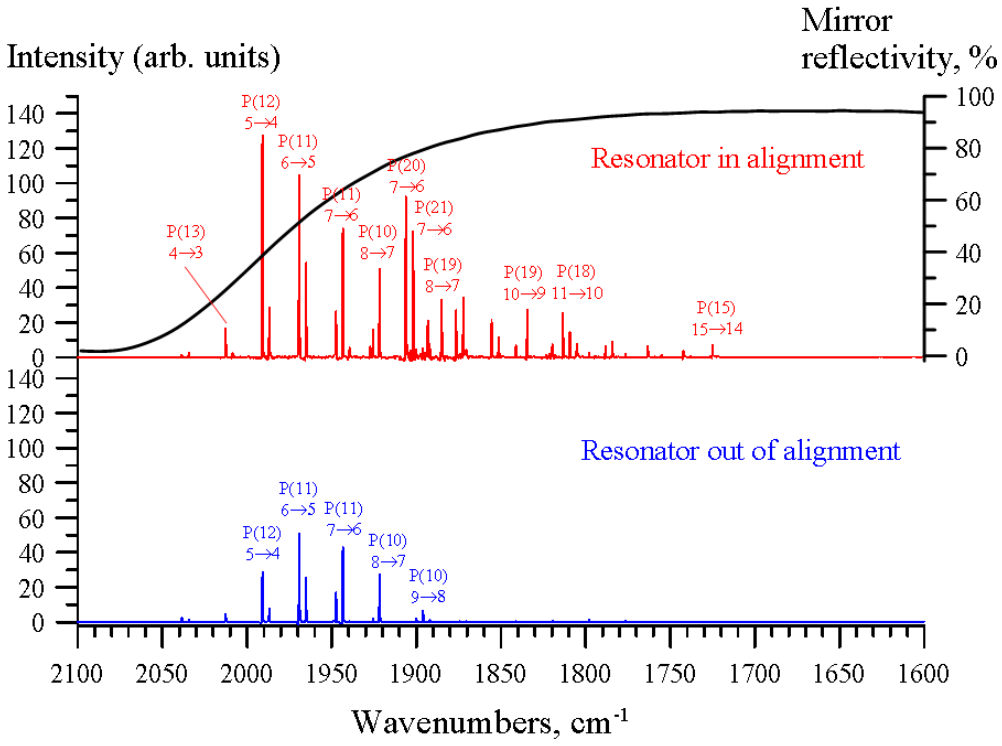

Figure 24. Laser (intracavity flux) spectra measured with the resonator in alignment (top) and out of alignment (bottom), at the conditions of figure 22 (3% CO in Ar, P = 10 Torr, T = 335 K). Additional laser lines generated in the optically pumped cell are shown in red.